AFRL-AFOSR-VA-TR-2024-0036

Scaling the Output Power of Monolithic Phase-Locked Arrays of Quantum Cascade Lasers

Mawst, Luke
UNIVERSITY OF WISCONSIN SYSTEM
21 N PARK ST STE 6301
MADISON, WI, 53715
USA

11/22/2023
Final Technical Report

Air Force Research Laboratory
Air Force Office of Scientific Research
Arlington, Virginia 22203
Air Force Materiel Command

REPORT DOCUMENTATION PAGE

PLEASE DO NOT RETURN YOUR FORM TO THE ABOVE ORGANIZATION.

1. REPORT DATE	2. REPORT TYPE	3. DATES COVERED	
20231122	Final	START DATE 20190915	END DATE 20230913

4. TITLE AND SUBTITLE
Scaling the Output Power of Monolithic Phase-Locked Arrays of Quantum Cascade Lasers

5a. CONTRACT NUMBER	5b. GRANT NUMBER	5c. PROGRAM ELEMENT NUMBER
	FA9550-19-1-0385	61102F
5d. PROJECT NUMBER	**5e. TASK NUMBER**	**5f. WORK UNIT NUMBER**

6. AUTHOR(S)
Luke Mawst

7. PERFORMING ORGANIZATION NAME(S) AND ADDRESS(ES)
UNIVERSITY OF WISCONSIN SYSTEM
21 N PARK ST STE 6301
MADISON, WI 53715
USA

8. PERFORMING ORGANIZATION REPORT NUMBER

9. SPONSORING/MONITORING AGENCY NAME(S) AND ADDRESS(ES)	10. SPONSOR/MONITOR'S ACRONYM(S)	11. SPONSOR/MONITOR'S REPORT NUMBER(S)
Air Force Office of Scientific Research 875 N. Randolph St. Room 3112 Arlington, VA 22203	AFRL/AFOSR RTB1	AFRL-AFOSR-VA-TR-2024-0036

12. DISTRIBUTION/AVAILABILITY STATEMENT
A Distribution Unlimited: PB Public Release

13. SUPPLEMENTARY NOTES

14. ABSTRACT
We are addressing the key challenges remaining to realize high brightness (i.e., near diffraction-limited beams) arrays with multi-watt (>5 W) QCW/CW average output powers. We have demonstrated QCL arrays that employ MOCVD regrowth for complete current confinement to the element regions, with improved device efficiency. Working with industrial collaborators, we also fabricated reverse-tapered single-spatial-mode buried heterostructure QCL lasers with coherent output power of 1.6 W QCW, with virtually no beam steering. Parallel efforts use frequency domain and steady-state thermal reflectance measurements to determine the thermal conductivity of the materials comprising the QCL structures continued. We have completed characterization of the cross-plane thermal conductivity of the QCL active region superlattice materials as a function of temperature and interface density. These studies give us new insights into phonon transport in SL materials relevant to QCL active regions. Finally, we performed preliminary high-spatial resolution X-ray mapping of the QCL facet during device operation. These techniques give us insights into strain fields and degradation pathways in the QCL.

15. SUBJECT TERMS

16. SECURITY CLASSIFICATION OF:			17. LIMITATION OF ABSTRACT	18. NUMBER OF PAGES
a. REPORT U	b. ABSTRACT U	c. THIS PAGE U	UU	32

19a. NAME OF RESPONSIBLE PERSON	19b. PHONE NUMBER *(Include area code)*
JOHN LUGINSLAND	000-0000

Standard Form 298 (Rev.5/2020)
Prescribed by ANSI Std. Z39.18

Scaling the Output Power of Monolithic Phase-Locked Arrays of Quantum Cascade Lasers
(Final Report)

Luke J. Mawst (PI) and Dan Botez (Co-PI)
University of Wisconsin-Madison

Brian M. Foley (subaward PI), Venkatraman Gopalan (subaward Co-PI)
The Pennsylvania State University

Start Date: Sept. 15, 2019
End Date: Sept. 14, 2023 (under NCE)
FA9550-19-1-0385

Executive Summary: Coherent power scaling of mid-infrared (IR)-emitting quantum cascade lasers (QCLs) to the multi-watt range remains a significant challenge. Our approach employs phase-locking of multiple antiguided QCLs on chip using resonant leaky-wave coupling to achieve multi-watt range output powers with near-diffraction-limited (D.L.) beams. Such devices require a multi-step etching and crystal growth process to fabricate the lasers. We have previously used metalorganic chemical vapor deposition (MOCVD) to realize leaky-wave coupled QCLs emitting at 4.7 μm, which operate to over 5 W peak-pulsed (low-duty-cycle) power with a D.L. beamwidth. We are addressing the key challenges remaining to realize high brightness (i.e., near diffraction-limited beams) arrays with multi-watt (>5 W) QCW/CW average output powers. By the third year, we have demonstrated QCL arrays that employ MOCVD regrowth for complete current confinement to the element regions, with improved device efficiency. Working with industrial collaborators at DRS Daylight Solutions (Madison, Wisconsin), we also fabricated reverse-tapered single-spatial-mode buried heterostructure QCL lasers with coherent output power of 1.6 W QCW, with virtually no beam steering. Beam quality and beam stability were characterized in collaboration with Intraband, LLC (Madison, WI). Parallel efforts use frequency domain and steady-state thermal reflectance measurements to determine the thermal conductivity of the materials comprising the QCL structures continued. By the third year, we have completed characterization of the cross-plane thermal conductivity of the QCL active region superlattice materials as a function of temperature and interface density, and in collaboration with Prof. Irena Knezevic (UW-Madison) correlated these data with a three-dimensional finite-difference time-domain (FDTD) solution to the elastic wave equation, in which the rms roughness and correlation length at the heterointerfaces are varied. These studies give us new insights into phonon transport in SL materials relevant to QCL active regions. Additional studies were conducted, showing that strain also plays an important role in the thermal conductivity properties of the SL materials, but further studies are needed to fully map out the effects of strain. We also completed studies on the thermal conductivity of n:InP and Fe:InP, since both materials are utilized in forming the optical waveguide and current confinement for QCL devices. Finally, we performed preliminary high-spatial resolution X-ray mapping of the QCL facet during device operation. These techniques give us insights into strain fields and degradation pathways in the QCL.

Program Objectives:

The overall goal of the proposed 3-year program is to develop phase-locked arrays with average output powers > 5 W, emitted into a near-D.L. beam pattern under QCW/CW operation.

Approach:

- Develop phase-locked laser array configuration with improved current-injection efficiency.
- Perform analysis of array performance and the dependence on scaling the aperture width and number of active stages
- Employ higher wall-plug efficiency QCL active materials: Step-Taper Active (STA) Region with Resonant Extraction. Such active materials are under development in related projects, but ultimately can be employed within the phase-locked array structure studied in this project.

- Thermal management for QCW/CW operation and mitigation of thermal lensing
- Develop improved thermal models for QCL: Experimental quantification of QCL material thermal-conductivity properties

Key results (details under Accomplishment section):

- Developed first phase-locked leaky-mode arrays with *complete current confinement* to the element regions. Such devices demonstrated up to 10W pulsed output power from 3-element arrays. This work is critical for future work for realizing higher performance devices.
- Investigated beam stability in BH QCLs and the dependence of aperture width.
- Demonstrated a novel reverse taper QCL with QCW output powers of >1.6 W and high beam stability. We are continuing to collaborate with industry partners Intraband LLC, and DRS Daylight Solutions to further develop these sources.
- Completed a comprehensive study on the thermal conductivity of the QCL active region and associated waveguide materials.
- Performed initial studies on facet stress under QCL operation using high-resolution x-ray diffraction measurements. This initial data allowed us to refine out measurement techniques for future studies in this area.
- Performed microanalysis of InGaAs/AlInAs QCL active regions using Atom Probe Tomography (APT) to establish for the first time the interface roughness parameters needed to accurately model device performance.

Status of Effort:

During the course of this project, we have successfully developed the fabrication methods for realizing the QCL phase-locked arrays with improved current injection efficiency and demonstrated experimentally two separate viable approaches; 1) proton implant within the array interelement regions of the array, and 2) completed etching through the active region within the interelement regions, followed by semi-insulating regrowth. Working closely with our industrial collaborators, DRS Daylight Solutions and Intraband LLC, we also established the criteria for achieving beam stability in buried heterostructure QCLs and investigated scaling the coherent power by employing a reverse-taper geometry, achieving ~1.6 W QCW from such devices with high beam quality and no significant beam steering.

We completed a thermo-reflectance measurement study to extract the cross-plane thermal conductutivity properties of strain-compensated InGaAs/AlInAs superlattice (SL) materials comprising the QCL. In collaboration with Prof. Irena Knezevic (UW-Madison), the measurements are found to be in good agreement with a three-dimensional finite-difference time-domain (FDTD) solution to the elastic wave equation, in which the rms roughness and correlation length at the heterointerfaces are varied, and the parameters yielding best agreement with experiment are determined using machine learning. Both the experimental measurements and the simulations demonstrate the existence of a minimum in the cross-plane thermal conductivity as a function of interface density, which is evidence of a crossover from incoherent to coherent phonon transport as the interface density increases.

Experiments were also performed to establish the thermal conductivity of n:InP and Fe:InP, which are used to form the optical waveguide and current blocking layers in BH QCLs.

Experiments were performed on interface roughness of QCL active regions by employing atom probe tomography (APT). These studies established for the first time that each interface within the QCL active can have differing roughness and correlation lengths, which directly impact interface roughness (IFR) scattering and limit device performance. These efforts set the stage for more comprehensive APT studies to fully characterize the in-plane and axial IFR parameters.

We experienced significant MOCVD equipment downtime during 2021/2022, which was aggravated by the Covid-19 staff restrictions within our laboratory facilities. While those issues were resolved, we requested a NCE due to these delays.

Accomplishments/New Findings:

Current-Injection Efficiency Optimization for QCL Arrays

During this project, we experimentally demonstrated two separate approaches to improve the current injection efficiency of the QCL array devices: 1) proton implant within the array interelement regions of the array, and 2) completed etching through the active region within the interelement regions, followed by semi-insulating regrowth.

Proton Implant for current confinement:

We carried out research on applying proton implant on our array devices for achieving efficient current confinement to the array element regions. We previously demonstrated (with collaborators at AFRL) the conversion of the InGaAs/InAlAs QCL active-region material into an effective current-blocking layer via proton implantation. In the current project, we demonstrate the effectiveness of proton implantation on a three-element phase-locked array of ~5.3μm-emitting quantum cascade lasers fabricated by a two-step MOCVD process. Based on our design simulations, we used a 35-stage, ~5.3 μm-emitting QCL structure grown by MOCVD. The active layers were separated by a thin InP spacer that improved laterally removing heat and act as a base layer for the regrowth in the interelement. InP:Fe and $In_{0.53}Ga_{0.47}As$ layers, of about 1.8 μm and 0.5 μm thickness at the center of the interelement regions, were then preferentially regrown by MOCVD in the interelements and outer trenches by using the silicon nitride mask employed for trench etching. The lower active region was implanted with a dose of 5×10^{14} cm^{-2} protons at 450 keV. The implantation reduces the electron concentration in the highly strained implanted InGaAs/InAlAs superlattice material by creating deep levels that trap carriers, resulting in an effective current blocking layer, as shown in Fig 1. A thick photoresist of ~14 μm was used as the implant mask to protect the un-implanted regions, although there is a slight misalignment of the mask to the underlying array.

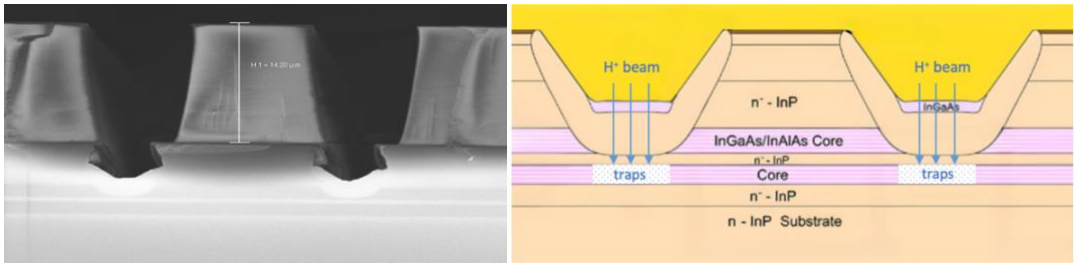

Fig 1. Cross-section SEM image of photoresist mask on top of array prior to implantation, and illustration of proton implantation into the array interelement regions.

Significant improvements of device performance are demonstrated. Fig 2(a) shows the light-current (L-I) curves of implanted 3-element arrays and a representative 3-element un-implanted array, in pulsed operation (200 ns-wide pulses, 20 kHz repetition rate). For the un-implanted 3-element curved array device, the threshold current is 5.48 A. The threshold currents of implanted devices are as low as 3.26 A, reflecting that the current is blocked in the implanted interelement regions. The slope efficiency is 1.74 W/A, and the wall-plug efficiency is 4.1%; both are improved compared to 1.47 W/A, and 3.1% for the un-implanted device. The measured far-field beam pattern near threshold current is a single-lobe with FWHM 6.67° as shown in Fig 2(b), indicating in-phase mode operation with near-diffraction-limited beam. The beams broaden (FWHM 7.65°) at higher drive currents due to the onset of adjacent modes reaching threshold.

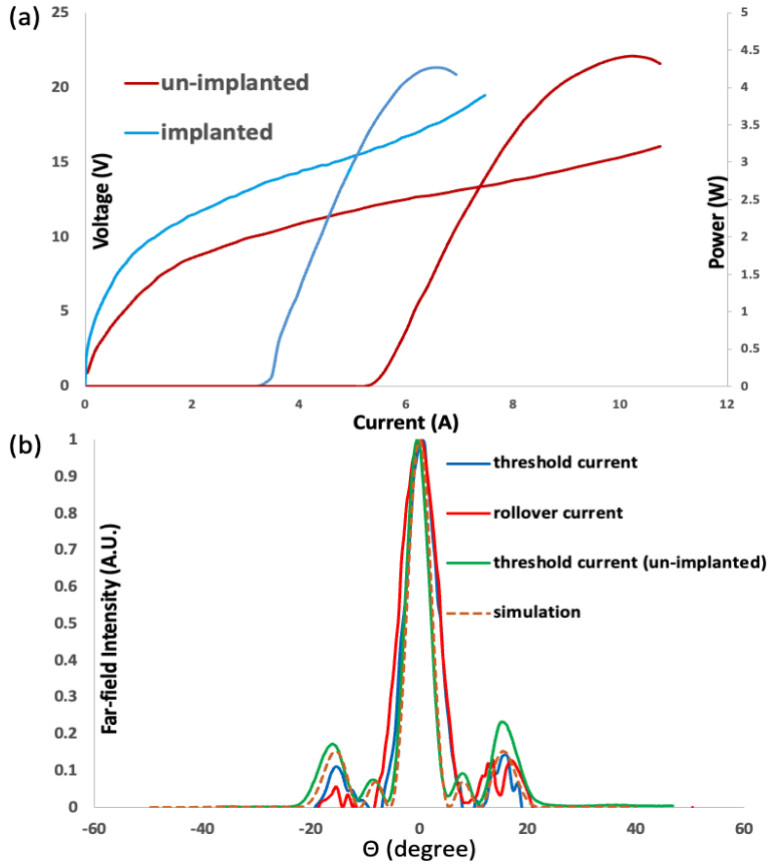

Fig 2. (a) Measured L-I-V data for implanted and un-implanted devices under short-pulse drive. (b) Far-field measurement result at near threshold (4 A) and roll-over point (8 A) driven current, and comparison to the simulation result.

The simulations of a 3-element curved array were carried out using COMSOL to find the expected current threshold and fabrication tolerance for the existing design. As shown in Fig 3, simulations confirm that these initial devices were non-resonant. SEM images indicate that the actual etched interelement region width is S_t~3.2 μm, larger than the target width needed to achieve resonance (S_t~2.5 μm). As a result, there is non-optimal discrimination against competing array modes. The simulated far-field mode profile has FWHM 4.99°, very close to the measured value 6.67°. The other modes introduce the multiple lobes at far-field, indicating the far-field beam broadening we observed at higher driven intensity.

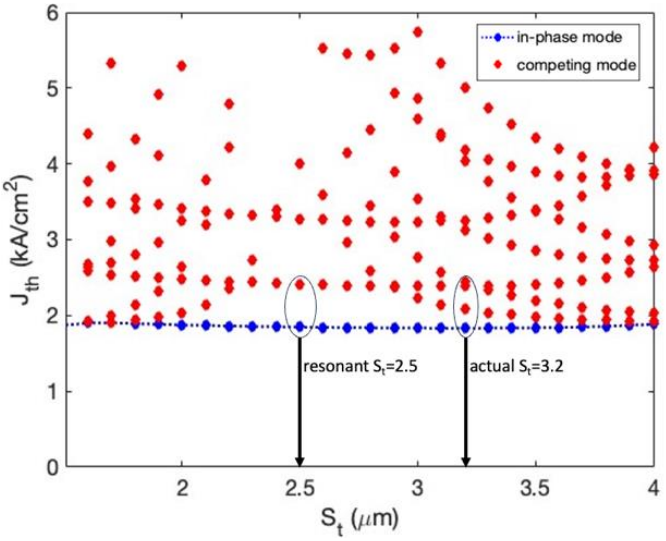

Fig 3. Threshold-current density (J_{th}) curves vs. the width of interelement regions (S_t), in which the curves of in-phase mode and competing modes are labeled.

These results indicate that large vacancy concentration introduced by the implantation in the lower core region making it an effective current-blocking layer. The implantation was performed on a sample of our prior QCL design originally grown in 2018. We believe it can be applied on our latest QCL designs, which should provide better performance. To continue, the regrowth of the interelement region is still a challenge needs to be further optimized, as discussed below.

New design curved array with high refractive index and high field-overlap parameter:

To further improve the performance of the phase-locked arrays of QCLs, we have designed an improved curved array structure with high refractive index and high over-lapping parameter, using an improved QCL active region base. The simulation indicates the field-overlap parameter to be 41% (26% for the previous design), and refractive index to be 0.125 (0.097 for the previous design).

In our fabricated phase locked arrays, the interelement regions were regrown an iron-doped InP current blocking layer, then followed by a high-index $In_{0.53}Ga_{0.47}As$ layer. The index difference between the element and interelement regions should be large enough ($\Delta n > 0.05$) for the in-phase mode operation. The non-resonant modes have large intensity in the lossy interelement regions, and the in-phase mode is resonant in the element regions. So, the

devices are favored to emit in-phase mode. The field-overlap parameter $|\kappa|^2$, calculated $\kappa = \int_{-\infty}^{\infty} E_{y1}^*(y)E_{y2}(y)dy$, where E_{y1} and E_{y2} are the electric field amplitudes of the modes in the two regions. A higher field-overlap value improves the modes coupling between element regions and the lossy interelement regions, resulting in an improved intermodal discrimination and uniformity of intensity across the devices.

The new design is shown in Fig. 4(a). The element regions apply the newest 5L active region design, aiming at wavelength of 4.7 um. It has 40 stages in total (30 stages for upper active region, and 10 stages for the lower region), separated by a 0.5 um InP spacer layer for heating dissipation. The regrown high index $In_{0.53}Ga_{0.47}As$ layer is 0.8 um, and the iron-doped InP 1.2 um. As shown in Fig. 4(b), the new designed array device has effective index of 3.2392 and 3.3643 in the element and interelement region, forming an index step Δn = 0.125. The calculated field-overlap is 41%, the highest value we have ever obtained for array devices.

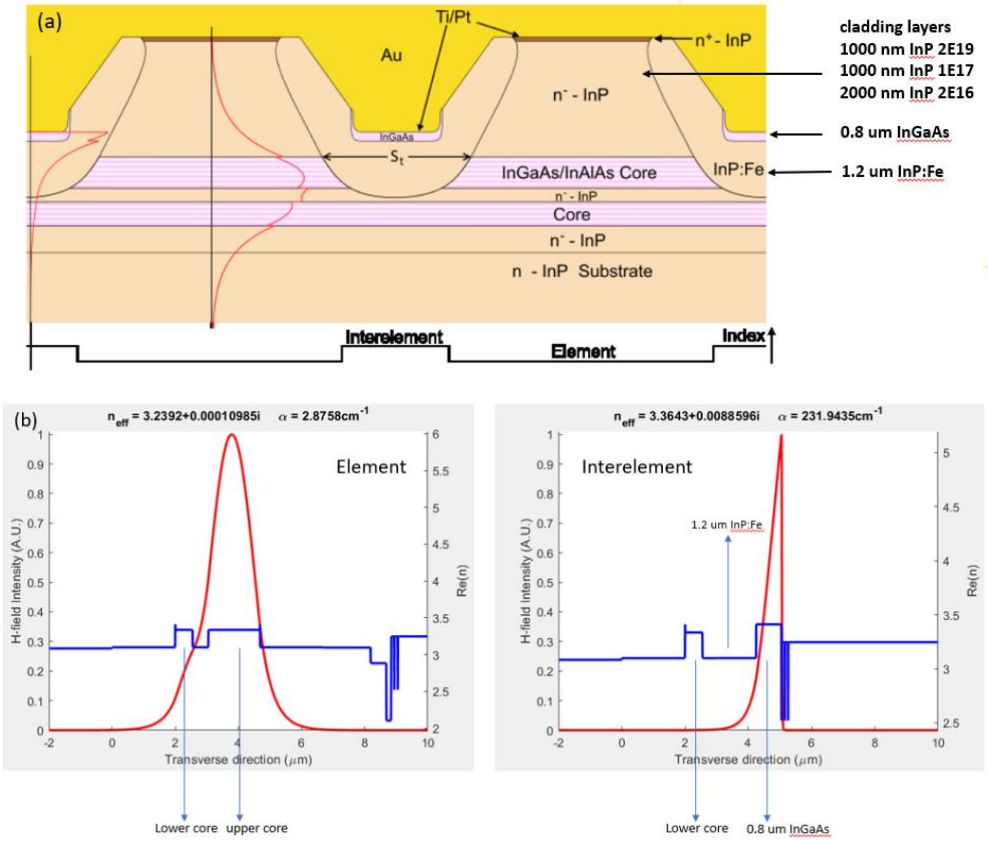

Fig 4. (a)Cross section illustration of the newly designed curved array structure. (b)Electric field amplitudes of the modes in the element and interelement region, respectively.

The interelement regions and outer trenches were etched by ICP. We used an optimized ICP recipe which uses BCl3/Cl2/H2/Ar as etch gases under high temperature (225°C). After ICP etch, an extra HBr-based wet etch was performed to create a smooth concave bottom. The selective regrowth procedure was done at UW using MOCVD system, followed by the conventional insulation layer and metal contacts deposition. The devices were mounted, and wire bonded on copper heat sink for the measurements. A representative fabricated device is shown in Fig 5. The geometry of regrown layers turns out to be perfect. We see no issues of any processing steps. Unfortunately, these devices failed to emit light. All the devices

behave like resistors. We analyze that the reason is the iron-doped regrown layer was not blocking the current. The current was leaking through the structure from the wide trench regions, or from the sidewalls on both sides outside the element regions. To solve this problem, we must continue to optimize the growth conditions for the regrown layers.

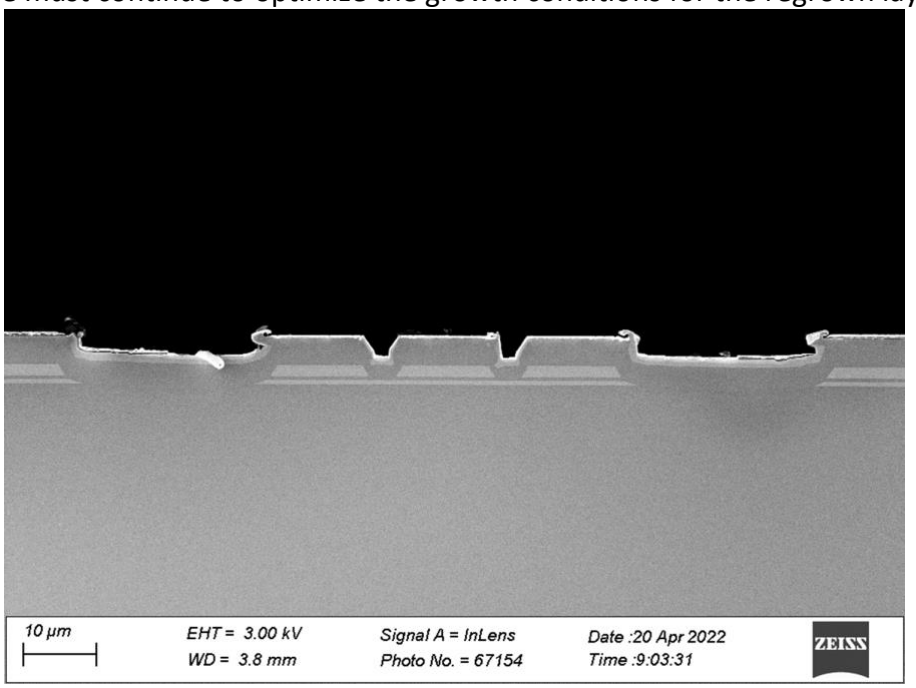

Fig 5. SEM image of the cross section of the 5L-base curved array.

Current confinement achieved through etch and regrowth: Arrays fabricated without lower active region layers:

We have continued collaborations with DRS Daylight Solutions throughout this project, to perform the MOCVD regrowth in the fabrication of our phase locked QCL arrays. While the phase-locked arrays provide a viable approach to scale the brightness of QCLs, the fabrication processes are more complex and the regrowth conditions stricter. DRS has already developed effective regrowth conditions for the current blocking iron-doped InP layer, although they did not previously utilize a ICP teched ridge (as needed for the array structures under development in this project). The base QCL materials were pre-prepared by DRS, which have 40-stage active regions with no spacer in the middle. This was also the first time that we have fabricated curved arrays using full 2" wafers for regrowth, and shows the potential for transferring the array fabrication process to larger area wafers. Note that all prior array regroiwths carried out at UW-Madison were carried out on ¼ of a 2" diameter wafer. Also, in this process run, the whole active layer must be etched through before performing the regrowth, as shown in Fig 6, since there is no lower active core in this design. The advantage of etching through the active region compared to etching only the top-active is that there is no current-spreading in the lower-active region, and improved lateral thermal conduction which is critical for the device to maintain the in-phase mode operation.

In the second year of this project we have achieved high power devices with more than twice the peak power than our previous partially-etched arrays, indicating improved current confinement of the semi-insulating Fe:InP. The output power would continue to increase if driven at higher currents. However, the device was shorted at 14 A current for some reason. We analyze that the shortage was due to the breaking-down of the thin regrown Fe:InP layer between the ridges. To address these issues, we modified the etching process by deliberately over-etching the inter-element regions, followed by a longer time HBr wet etching. The target thickness of Fe:InP was increased from 1 um to 3 um to compensate the deeper trenches. Due to the unpredictability of regrowth rate, the regrown materials exceed the ridge surface, as shown in Fig 6(a). Metal contacts were cut off at these protruding locations, which produced enormous heats. Most devices died at high driven currents. As shown in Fig 6(b), a large damaged area occurred at these heating traps.

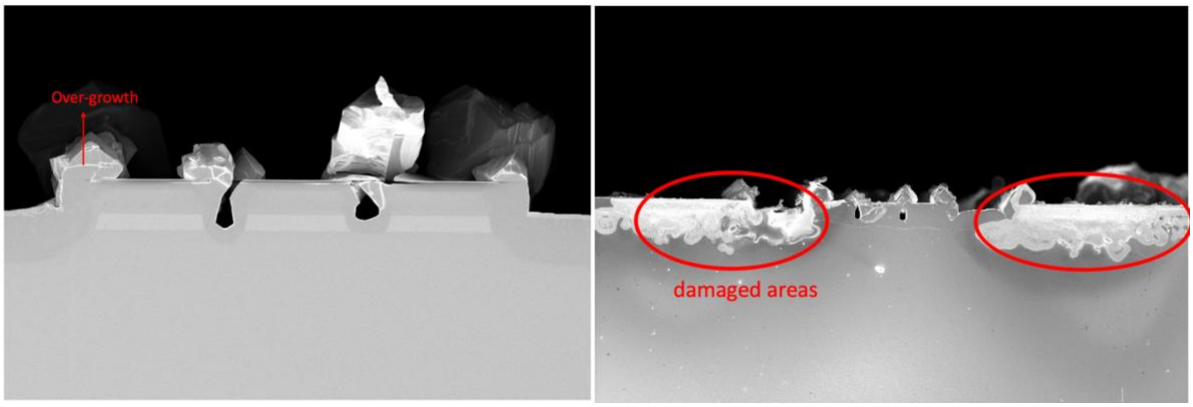

Fig 6. Cross section SEM images of the DRS-regrown 3-element curved array device. (a) before testing; (b) after testing.

Fig 7 shows the comparison of the measured light-current-voltage (L-I-V) curves of three-element arrays in pulsed operation (200 ns-wide pulses, 200 kHz repetition rate). The threshold current for the latest devices is 3.1 A, less than half of the threshold current from last year's regrowth. The peak output power reaches 11.8 W, and a maximum pulsed wallplug efficiency of 8% at 7.9 A driven current. As a comparison, 3 mm-long ridge waveguides with HR-coated back facets and uncoated front facets were fabricated from the same QCL growth. The devices from last year have a threshold current of ~8.0 A, a maximum pulsed wallplug efficiency of 4%, with ~10.5 W peak output power.

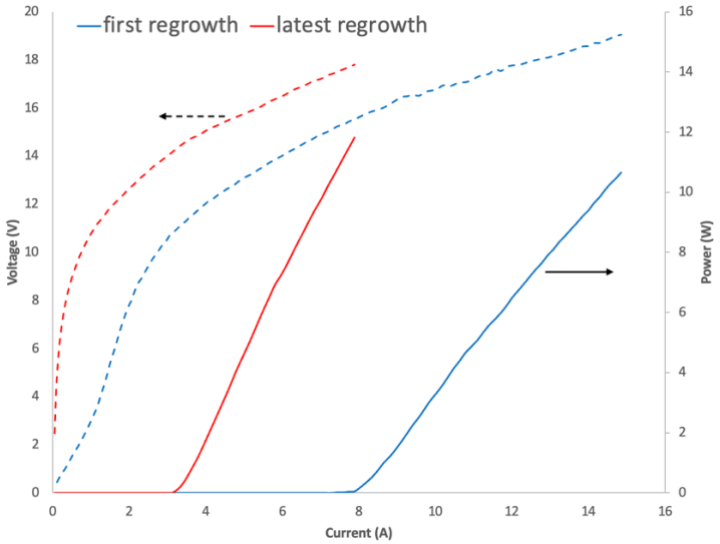

Fig. 8. Comparison of DRS etched-through 3-element array from first regrowth last year and the latest regrowth. The measurement was performed under short-pulse drive conditions of 200 ns-wide pulses, 20 kHz repetition rate.

This is the first time such a high output power (>10 W) was achieved for the phase-locked array devices. Some issues remain before we can achieve reliable devices. The next step is to modify the growth conditions to ensure the regrowth morphology and good metal contacts. The heating issue will be addressed by adding gold-plating, and mounting the device epi-down for better heating dissipation. We have recently developed the thick Au plating procedure at UW and it is ready for application to array structures and reverse taper devices in future projects.

Large-aperture (7-12 element) Phase-locked QCL arrays with reduced number of active region stages

Optimization studies were performed focused on reducing the number of stages of the active region so reduce the device thermal resistance and operating voltages. The InP spacer in the core was used to help removing heat in lateral direction at a cost on transverse optical-modal confinement. However, for the active regions below 25 stages, the 0.5 µm InP spacer would introduce extra losses to the device, so we have removed the spacer and the new structure is given below:

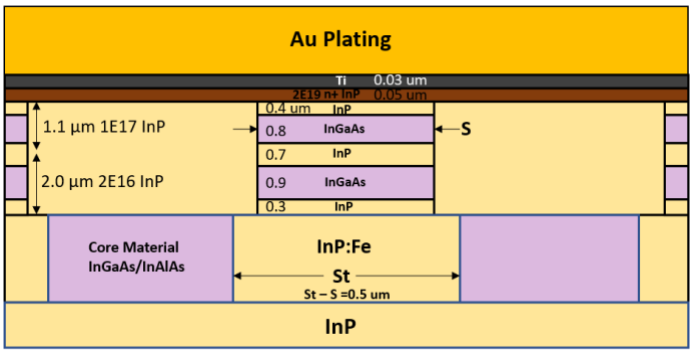

The model used to predict the CW performance of buried heterostructures (BHs) was modified to allow it to predict the CW or quasi-CW performance of the array. In previous array

simulations, we assumed that the array structure in this model has an internal loss 1.5 cm^{-1} , i.e. higher than a BH device. However, the output powers are highly sensitive to the loos value taken in the simulations.

Results are summarized below for CW operation:

Planar QCL Phase-Locked Array under CW operation:
35 stages: The resulting 7-element design has a front facet reflectivity of 5.3%, and an injector sheet doping of 1.45×10^{11} cm^{-2}. The predicted maximum CW output power for this device is 6.46 W at a current of 15.65A and voltage of 15.52 V, for a wallplug efficiency of 2.7%, while the maximum power in pulsed operation is 19.7 W at a current of 21.35 A. Its thermal resistance is 0.58 K/W.
30 stages: The device has a front facet reflectivity of 2%, and an injector sheet doping of 1.33×10^{11} cm^{-2}. The predicted maximum CW avg. output power for this device is 5.62 W at a current of 15.45A and voltage of 13.68 V, for a wallplug efficiency of 2.7%, while the maximum power in pulsed operation is 14.9 W at a current of 19.54 A. Its thermal resistance is 0.59 K/W.
25 stages: The device has a front facet reflectivity of 2.75%, and an injector sheet doping of 1.57×10^{11} cm^{-2}. The predicted maximum CW avg. output power for this device is 4.22 W at a current of 18.9A and voltage of 12.2 V, for a wallplug efficiency of 1.8%, while the maximum power in pulsed operation is 12.4 W at a current of 23.77 A. Its thermal resistance is 0.53 K/W.
20 stages: Due to its high losses, the CW output power is very low. The simulated data resulted from the COMSOL couldn't fit in well with reference P-I curves of the BH devices. Further optimization must be done on 20-stage device to reduce this loss issue.

Alternate approaches to power scaling: Large-area (Tapered) QCLs

During the early part of this project, we investigated the beam stability and beam quality of single stripe buried heterostructure QCLs. This work helped establish the criteria for stripe width to reduced beam wander. We found that stripe widths larger than ~4 microns led to significant beam instabilities. Since these initial investigations, we have continued our study on the fabrication of novel buried heterostructure (BH) QCLs. Given the complex fabrication processes of the phase-locked arrays, we are also investigating other means to scale the device area and hence the maximum output power while maintaining beam quality.

The new tapered QCLs were grown and fabricated by our industrial collaborators, DRS Daylight Solutions. They used an optimized tapered structure similar to what we reported last year. A schematic top-view of the reverse-taper QCL structure is shown in Fig. 9 (a). The device under consideration has a total device length of 6 mm, where the length of the straight narrow section ($L_{straight}$) is 2 mm, and the length of the tapered region (L_{taper}) is 3 mm. The equation for the width of the taper is $W = \sqrt{\frac{2\alpha\lambda z}{n_{eff}} + W_0^2}$, where α is a constant < 1 and W_0 is the width of the narrow section. Reverse-taper devices, along with a regular straight buried-heterostructure (BH) device as a reference, were fabricated with a narrow section of W_0 = 3.4 μm with taper widths (W = 9.7 or 14.6 μm).

The tapered device with a tapered aperture width of 9.7 μm was mounted epi-side down using indium solder to measure QCW/CW device characteristics. L-I-V characteristics and the beam stability of the devices were measured in QCW operation (500 μs pulse width and 1 kHz rep. rate). From the 2-D beam profiles Fig 9. (c), we can see that the beam is stable up to roll-over. The beam stability along the transverse direction (y) exhibits negligible angular deviations, which is expected since high-order modes are cut-off in that direction. Along the x-direction, the beam also exhibits negligible angular deviations, up to ~ 1.6 W QCW output power. The angular deviation along both the lateral (x) direction normally fluctuates more than that of the transverse (y) direction, since the device favors to operate multimode. But this new reverse-taper device has a beam deviation within < 0.02 mrad along both x and y direction, which corresponds to a ~ 0.2 cm targeting error over a 100 m distance. This value is more than 10 times smaller (~0.25mrad along x-direction) than the previous device from last year. These beam measurements were conducted in collaboration with Intraband, LLC (Madison, Wisconsin).

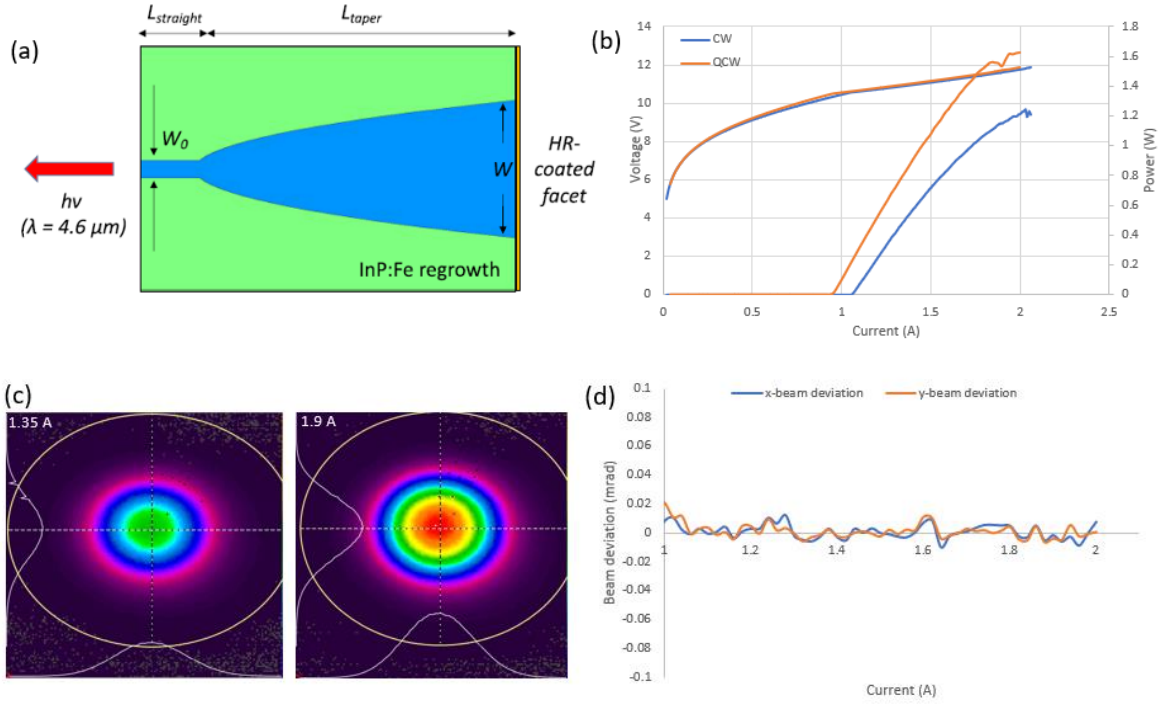

Fig 9. (a) Schematic top-view of the reverse-taper QCL structure; (b) Measured L-I-V data for representative reverse-taper devices under QCW (500 ns-wide pulses, 1 kHz rep. rate), and CW conditions. (c)Far-field beam profiles at near threshold and roll-over operating currents for the 9.7 um reverse-taper device under QCW drive conditions (500 ns-wide pulses, 1 kHz rep. rate). (d)Measured beam deviation along x and y-axis under QCW conditions.

These results of reverse taper BH QCLs indicate that this device structure can be utilized to scale the output power while maintaining good beam quality through mode filtering. Further optimization of the taper structures is needed to fully explore the geometrical parameter space for scaling the output powers further.

Thermal Metrology of Materials and Structures Pertinent to Quantum Cascade Laser (QCL) Arrays: Thermal Transport Studied Through III–V Alloy Superlattices reveals Incoherent-to-Coherent Crossover

Thermal transport in superlattices (SLs) has not yet been fully understood despite numerous experimental and theoretical investigations[1–8]. Given that the thermal management of thermoelectric energy converters, quantum cascade lasers (QCLs), and other optoelectronic devices based on SLs is vital for their optimal performance, it is essential to understand thermal transport in these systems. For example, in a SL systems such as the active region of midinfrared QCL grown on InP, which consists of hundreds of layers of alternating ternary materials InGaAs and AlInAs, thermal transport will depend on multiple parameters: periodicity, total sample thickness, interface properties, layer composition and strain, and, of course, temperature. The problem is complex because thermal transport is inherently broadband, with phonons of vastly different wavelengths (thus interacting strongly with vastly different spatial scales of disorder) contributing to thermal conductivity. On the one end are short-wavelength phonons, whose transport is largely incoherent and well described by a particle-like picture and the semiclassical Boltzmann equation. The SL period is larger than the mean free path for intralayer scattering due to alloy disorder and three-phonon scattering and scattering from random rough interfaces is a phase-breaking process. On the other end are long-wavelength phonons, capable of traveling across multiple periods without undergoing a phase-breaking process, and their transport is largely coherent. The Simkin-Mahan[9] model for thermal transport in SLs, which notably does not incorporate diffuse interface scattering, predicts a minimum in the thermal conductivity as a function of period, and this minimum indicates a crossover between predominantly incoherent transport at larger periods (lower interface densities, ID) and coherent transport at smaller periods (higher IDs).

We performed time-domain thermoreflectance (TDTR) measurements of the cross-plane thermal conductivity of $In_{0.63}Ga_{0.37}As/In_{0.37}Al_{0.63}As$ superlattices with interface densities ranging from 0.0374 to 2.19 nm^{-1} in the temperature range 80–295 K. The measurements were complemented by a three-dimensional finite-difference time-domain (FDTD) solution to the elastic wave equation, in which the rms roughness and correlation length at the heterointerfaces are varied, and the parameters yielding best agreement with experiment are determined using machine learning. Both experimental measurements and simulations demonstrate the existence of a minimum in the cross-plane thermal conductivity as a function of interface density, which is evidence of a crossover from incoherent to coherent phonon transport as the interface density increases. This minimum persists with increasing temperature, indicating the continued dominance of the temperature-independent interface and alloy-disorder scattering over the temperature-dependent three-phonon scattering in thermal transport through III–V alloy superlattices. When it comes to semiconductor SLs, a number of experimental and computational papers have reported on the thermal conductivity of group-IV SLs, while the work on III–Vs has largely focused on the SLs between two binaries[2–6,18–21]. In contrast, there have been few reports on the thermal conductivity of III-V alloy/alloy SLs, especially for the InGaAs/InAlAs material system, which is of great importance in optoelectronics[22,23].

In a published manuscript, we report on the TDTR measurement of the thermal conductivity as a function of ID (approximately 0.0374 to 2.19 nm^{-1}) at different temperatures

(80, 135, and 295 K), and the thermal conductivity as a function of temperature of strain-balanced $In_{0.63}Ga_{0.37}As/In_{0.37}Al_{0.63}As$ SLs relevant to QCLs. In addition, we used a three-dimensional finite difference time-domain (FDTD) solver for the elastic wave equation to calculate the thermal conductivity of $In_{0.63}Ga_{0.37}As/In_{0.37}Al_{0.63}As$ SLs. In these simulations, we varied the interface roughness and correlation length at the heterointerfaces within the SLs to investigate the sensitivity of the model and the data to interfacial mixing. Machine learning was used to determine the interface roughness and correlation length. The FDTD simulations are in good agreement with measurements below 295 K. We observe a minimum in the thermal conductivity as a function of ID for $In_{0.63}Ga_{0.37}As/In_{0.37}Al_{0.63}As$ SLs, which is evidence of incoherent-to-coherent phonon transport in alloy/alloy SLs and also corroborated via FDTD modeling.

TDTR was employed to measure the thermal conductivity of nine $In_{0.63}Ga_{0.37}As/In_{0.37}Al_{0.63}As$ SL samples. TDTR is a noncontact optical pump-probe technique mainly used to measure the thermal conductivity[26–29] and thermal conductance of solid/solid and solid/liquid interfaces[26,29–33]. A schematic of the experimental setup is presented in Fig. 10.

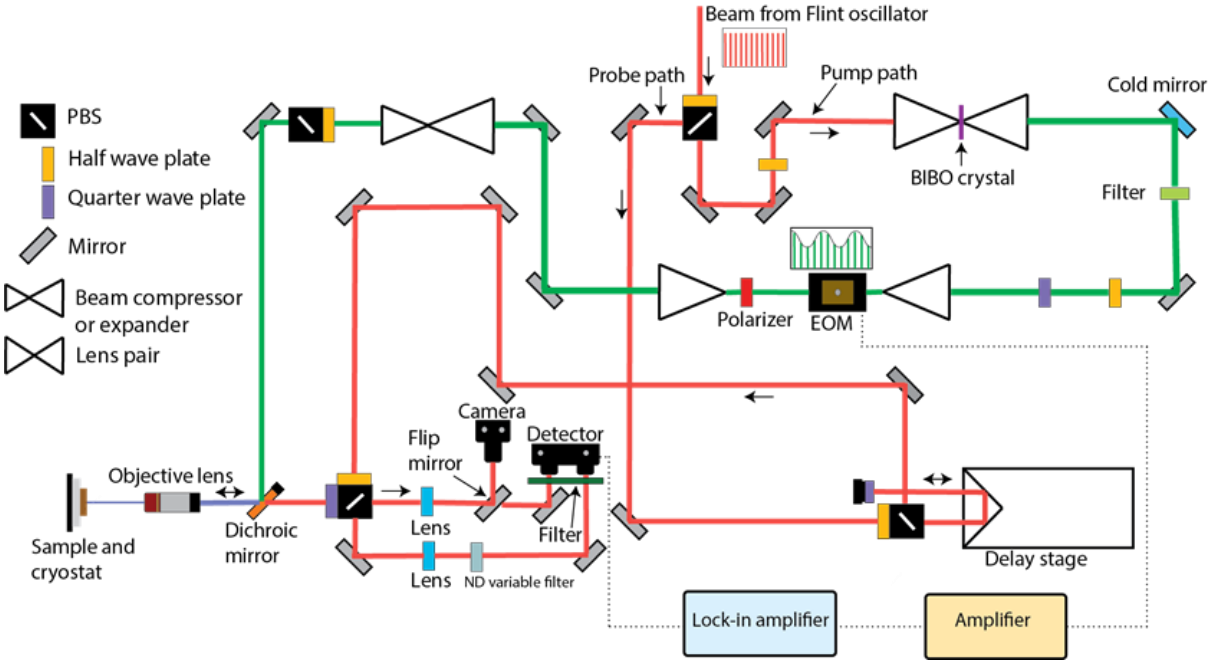

FIG. 10. Schematic of the time-domain thermoreflectance (TDTR) measurement system. The pump and probe beams are represented by green and red lines, respectively.

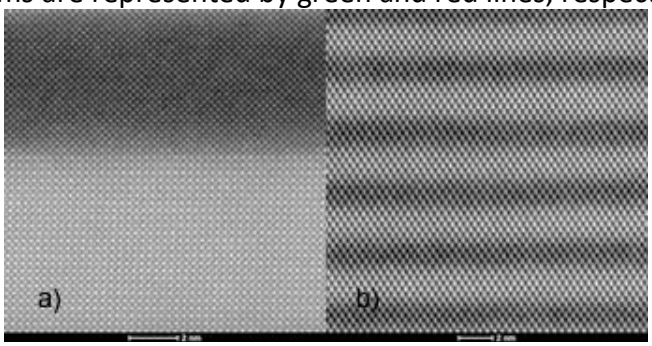

FIG. 11. STEM images of $In_{0.63}Ga_{0.37}As/In_{0.37}Al_{0.63}As$ SLs with different IDs. (a) STEM image shows good quality interface for the SL with ID of 0.151 nm^{-1}. (b) STEM image shows intermixing for the SL with an ID of 0.601 nm^{-1}.

The $In_{0.63}Ga_{0.37}As/Al_{0.63}In_{0.37}As$ SL samples under study were grown by low-pressure metalorganic vapor phase epitaxy (MOVPE). A STEM image of the SL layers is shown in Fig. 11. Table I lists the characteristics of each strain-balanced SL, such as layer thickness, indium content, ID, and layer thicknesses. The total thickness of the SLs was kept constant at approximately 212 nm because the scattering from boundary edges (and thus sample size) affects thermal conductivity. The ID values range from 0.0374 nm^{-1} to 2.19 nm^{-1}

Table I. Layer thicknesses, indium molar fraction, and interface density of the nine characterized SLs.

Characterized Samples (Superlattices)							
Samples	Layer A material	Thickness (nm)	In molar fraction	Layer B material	Thickness (nm)	In molar fraction	Interface density (nm^{-1})
1	InAlAs	20.8	0.37	InGaAs	32.7	0.63	0.0374
2	InAlAs	16.6	0.37	InGaAs	25.9	0.63	0.0471
3	InAlAs	13.4	0.37	InGaAs	22.0	0.63	0.0565
4	InAlAs	10.4	0.37	InGaAs	16.1	0.63	0.0755
5	InAlAs	5.23	0.37	InGaAs	8.05	0.63	0.151
6	InAlAs	2.64	0.37	InGaAs	4.01	0.63	0.301
7	InAlAs	1.32	0.37	InGaAs	2.01	0.63	0.601
8	InAlAs	0.580	0.36	InGaAs	0.886	0.62	1.36
9	InAlAs	0.323	0.36	InGaAs	0.590	0.59	2.19

Figure 12 illustrates the measured and calculated values of the thermal conductivity in two of the SLs (4, with ID=0.0755 nm^{-1}, and 7, with ID=0.601 nm^{-1}) as a function of temperature in the range 80–295 K. The error bars represent the uncertainty calculated due to the Al film thickness and the standard deviation of the four measurements. The experimental thermal conductivity values vary from 1.14–0.9 W m^{-1} K^{-1} at 80 K to 1.86–1.69 W m^{-1} K^{-1} at 295 K. In all samples, the thermal conductivity increases with increasing temperature as vibrational modes become energetically accessible, eventually saturating above approximately 295 K. The fact that the thermal conductivity approximately saturates above 295 K indicates that temperature-independent mechanisms such as interface roughness and alloy scattering dominate instead of three-phonon umklapp scattering that dominates in bulk materials.

Thermal transport in alloy SLs is simulated by solving the elastic wave equation using the finite-difference time-domain (FDTD) technique in the velocity-stress formulation, which we developed earlier[37]. The fact that the FDTD model agrees so well with experiment over a wide temperature range is an indirect proof that interface and alloy scattering remain

dominant over the strongly temperature-dependent three-phonon umklapp scattering up to high temperatures.

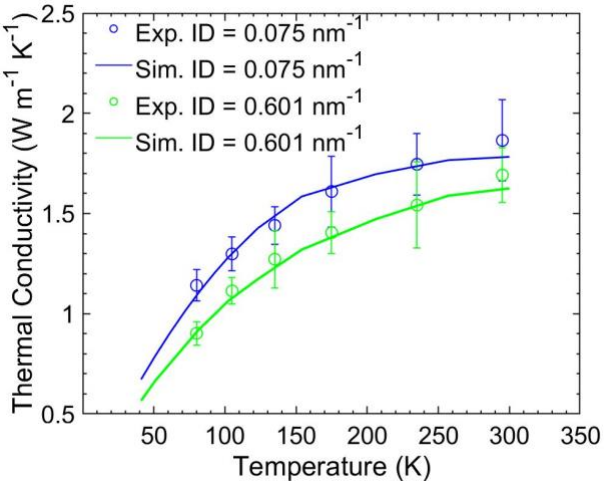

FIG. 12. Cross-plane thermal conductivity of InGaAs alloy SLs versus temperature at two IDs, 0.0755 nm^{-1} (blue) and 0.601 nm^{-1} (green), as obtained in experimental measurement with TDTR (open circles) and numerical simulation via FDTD (curves). Open symbols are experimental averages, and the error bars represent the uncertainty calculated due to the Al film thickness and the standard deviation of the four measurements.

Figure 13(a) illustrates the thermal conductivity as a function of ID at 80 K, 135 K, and 295 K. There is a clear minimum is in the thermal conductivity as a function of ID that persists to room temperature. This minimum represents a crossover from incoherent to coherent transport of thermal carriers moving in the cross-plane direction. Prior modeling work treating diffuse scattering at rough interfaces as a phase-breaking (coherence-destroying) process[9,40] predicted this dip at the point of crossover in SLs. In other words, when the ID is lower than that of the minimum, heat carriers scatter at the rough but individually resolved interfaces, a process that randomizes the phase of scattered waves, so transport ends up being largely incoherent. Conversely, as the ID increases past the minimum point, the SL structure begins to behave as a new, virtually homogeneous material. In this case, the heat carriers (especially long-wavelength ones) move coherently across the SL structure within the new digital alloy material. Our data supports this idea by noting that as the ID increased from ~0.0374 to 0.601 nm^{-1}, the thermal conductivity deviates from the thermal conductivity value measured in a quaternary alloy (denoted in dashed lines) that represents the control case of no interfaces. This deviation captures the additional reduction of thermal conductivity that is caused by interface scattering, which goes beyond the scattering within the alloy layers. As the ID crosses ~0.601 nm^{-1} and approaches the maximum of 2.1906 nm^{-1}, the thermal conductivity comes back up and recovers to the same magnitude from the quaternary alloy, consistent with the idea that when the thicknesses of the layers are on the order of the unit-cell size, the SL is effectively a homogeneous alloy. At this limit, the interfacial disorder permeates the entire SL making the structure essentially an alloy.[14]

In Fig. 13(b), we compare experiment to modeling results for thermal conductivity versus ID at 80 K. The model, which used an interface roughness of 0.4 nm and a correlation length of 4 nm, and **the experimental data are in excellent agreement**. The optimal interface roughness and correlation length were determined using machine learning (a neural network

analysis) based on our own FDTD simulation data. The relatively high roughness in the simulation has the same effect as the smaller spatial roughness obtained from experiments[39] combined with intermixing of binary alloys near the interfaces. Furthermore, by increasing the ID, the SL thermal conductivity approaches the thermal conductivity of the quaternary alloy. The resemblance can be seen in the insets of Fig. 13(b).

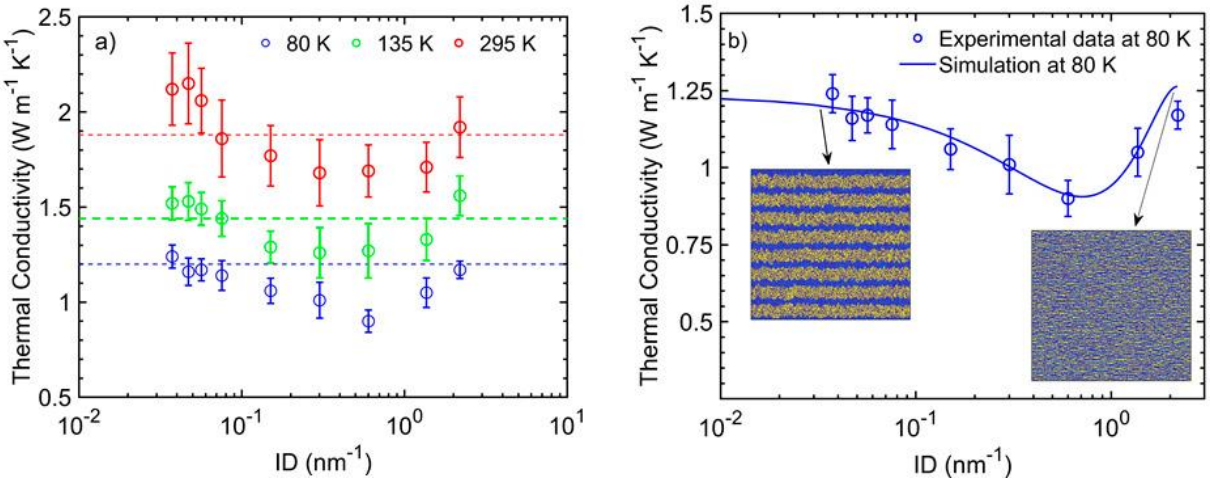

FIG. 13. (a) Experimental values of the cross-plane thermal conductivity at 80 K (blue), 135 K (green), and 295 K (red) versus ID ranging from 0.0374 to 2.19 nm^{-1}. The dashed horizontal lines represent the reference values for the bulk quaternary alloys of the same stochiometry as the SLs. (b) Experimental (open symbols) and modeling values (solid curve) for the cross-plane thermal conductivity as a function of ID at 80 K. Symbols are experimental averages and error bars are the standard deviation of four measurements.

Overall, this work contributes to the further understanding of the nature of thermal transport in SLs, particularly the relative importance of disorder (alloy and interface roughness) versus multiphonon processes in thermal transport through SLs, which has clear repercussions in the thermal management of electronic and optoelectronic devices.

Thermal Conductivity of Silicon Doped Indium Phosphide

During this project we also measured κ of thin-film Si-InP and Fe:InP, since these materials are used to construct the optical waveguide for the QCL, as shown in Fig. 14.

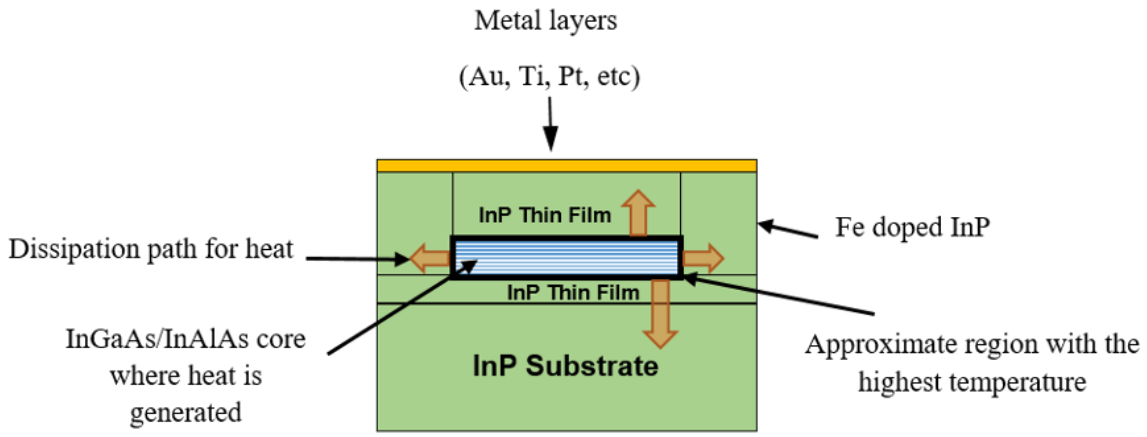

Fig. 14 Schematic diagram of a QCL BH cross-sectional view.

To broaden the understanding of the phonon scattering mechanisms at various temperatures, thermal conductivities were measured over a temperature range from 80 K up to 450 K, as well as film thickness (Fig 15, 16). Furthermore, this work focused on the film thicknesses and dopant concentration effects on κ, as it is essential for the design of QCL materials. We gained insight into the phonon scattering mechanisms' influence by applying the phonon-gas model. Through modeling efforts, the effects of the point-defect and boundary scattering mechanisms that ultimately influence thermal conductivity in InP-based materials were characterized, filling the knowledge gap regarding the thermal properties of materials that are pertinent to QCLs. After confirming that the phonon gas model matched experimental measurements, a sensitivity analysis was performed on κ as a function of thickness and carrier concentration which showed that although thickness has a more significant influence on κ than carrier concentration at the micron scale for all samples, point defects due to Si dopant atoms at high carrier concentrations of ~10^{19} cm^{-3}, as well as the presence of extended defects that are most likely present due to dopant saturation, have a significant impact on κ due to increased phonon scattering, decreasing κ by 40% or more.

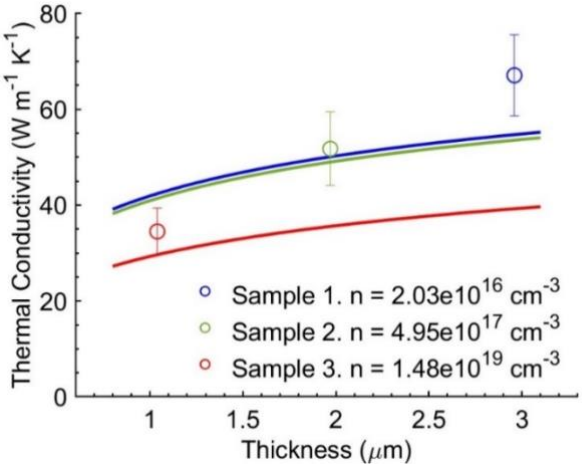

Fig 15. Measured κ of the Si-InP samples (circles) fabricated with varying thicknesses and carrier concentrations (n); solid lines represent the phonon gas model calculations of κ for different carrier concentration and thickness. The error bars represent the uncertainty calculated according to the Au (transducer) film thickness and the standard deviation of the three measurements.

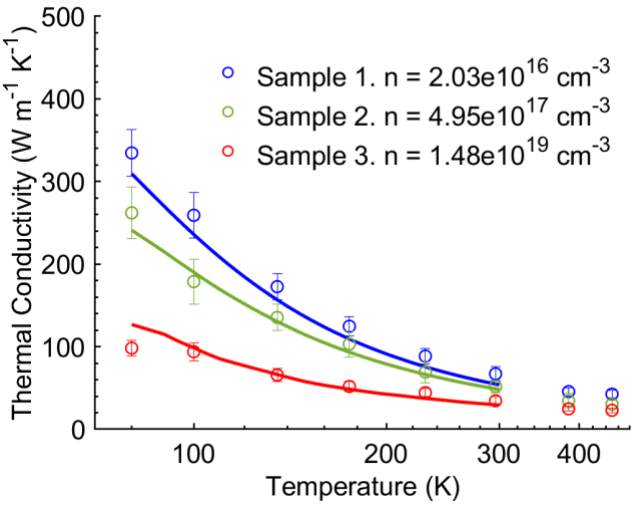

Fig 16 Measured κ for InP samples as a function of temperature at different thicknesses and carrier concentrations. The error bars represent the uncertainty calculated taking into account the Au (transducer) film thickness and the standard deviation of the three measurements.

We also aimed to better understand the effect of different mechanisms on the thermal conductivity of Fe-InP grown using HVPE at different temperatures (Fig 17), and iron concentrations (Fig. 18), which has not been previously reported in the literature. We investigated a Fe-InP sample with a thickness of 10 µm and iron concentration of 2.3×10^{18} cm^{-3}. In this study, we found that for film thicknesses greater than 1 µm, the overall sensitivity of thermal conductivity as calculated using the phonon gas model is greater than the concentration of the sample under study. As temperature decreases, the thickness sensitivity increases, and boundary scattering becomes more significant than impurity scattering. When iron doping reaches a certain concentration, thermal conductivity decreases significantly. The concentration value associated with "critical" concentration is approximately 3.6×10^{20} cm^{-3}.

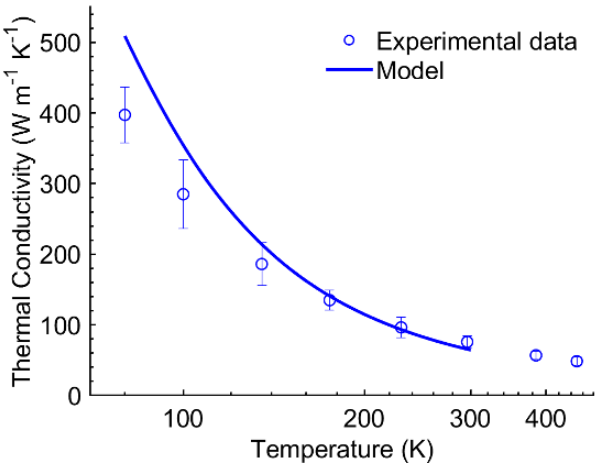

Fig 17 A comparison of experimental (open symbols) and modeling values for cross-plane thermal conductivity of Fe:InP at different temperatures.

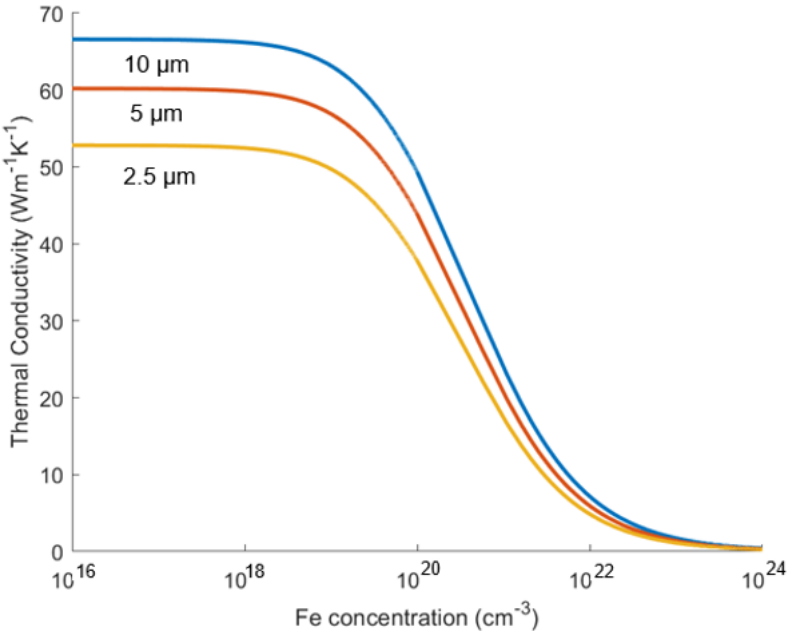

Fig 18 Thermal conductivity (Wm^{-1} K^{-1}) versus iron concentration (cm^{-3}) for three-layer thicknesses (10 µm, 5 µm, 2.5 µm).

In-operando XRD measurements on BH QCL devices:

The importance of *in-operando* characterization is two-folds: First, to improve the understanding of in-operando functions while comparing to the intended theoretical designs, and second, to uncover the degradation and failure mechanisms limiting the output power and the device energy efficiency. Thermal characterization is required to meet these challenges by interrogating the device structure and its physics. Prominently, under progressive high-power operation, it was observed that the active region of the QCL's becomes very hot relative to the surrounding material, sequentially leading to power output saturation, degradation of lasing spatial profile and spectral content, and ultimately leads to catastrophic mechanical fracture of the devices. Consequently, based on combining the experimental and theoretical results, thermal management in synergy with optoelectronic implementations will mitigate the existing challenges by improving the device fabrication routes by informing alternative design avenues.

In these initial experiments we employed high-resolution XRD measurements to probe the mechanisms of device degradation and failure. The general procedure for the experiment required us to measure rocking curve scans around the active region, with the X-ray beam aligned to the facets of the devices. The X-ray energy was fixed at 10 keV, while the X-ray microscopy at Bragg diffraction condition is performed under full field imaging conditions

(dark field) for X-ray imaging microscopy (XRIM) at beamline 33-ID of Advanced Photon Source at the Argonne National Laboratory in collaboration with staff, Dr. Zhan Zhang. Under optimized conditions of the instrument, the spatial resolution can reach 100-200 nm. With this setup, we chose a specific diffraction condition and performed scans to observe temporal behavior of the device under operation. The ultimate goal was to see whether there was any significant change in the diffraction pattern at the specific diffraction condition due to device heating.

As part of this study, we performed multiple tests with active cooling, where the submount temperature was held constant at 20°C, and one test without active cooling. When we used active cooling, we did not notice any significant change in the diffraction pattern for electrical power well above the threshold for lasing in QCL devices. One exception to this is when the intensity of the incident x-rays was too high, resulting in damage to the facet, Fig. 19. Subsequent measurements were performed with lower-intensity x-rays to avoid nondestructive X-ray imaging conditions. When we turned off the active cooling, we observed that the diffraction pattern widened as we increased the amount of current flowing through the device, until the device facet experienced a catastrophic failure which prevented us from being able to measure the diffraction pattern from that device (the device facet "blew out"). We expect that the device failed due to a combination of thermal stresses and x-ray induced damage, Fig. 20. The bright contrast in images is associated to spatial regions satisfying the Bragg diffraction condition simultaneously and include tilted and not tilted regions of the device due to local strains. Full interpretation of the data in the future will require image processing and modeling in conjunction with complimentary experimental results presented in the next section that employed hard X-ray nanoprobe for imaging of QCL devices.

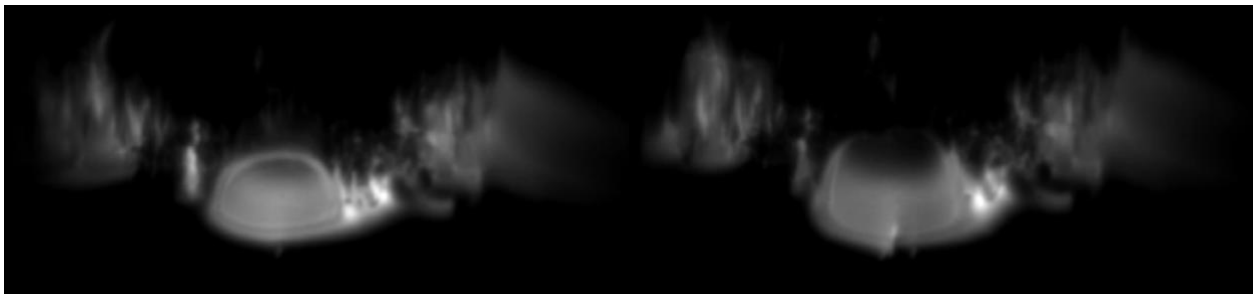

Figure 19: X-ray induced damage to the facet when the incident x-ray intensity was too high and the bright contrast in the active region and around it is irreversibly changed in the right image with respect to pristine state on the left.

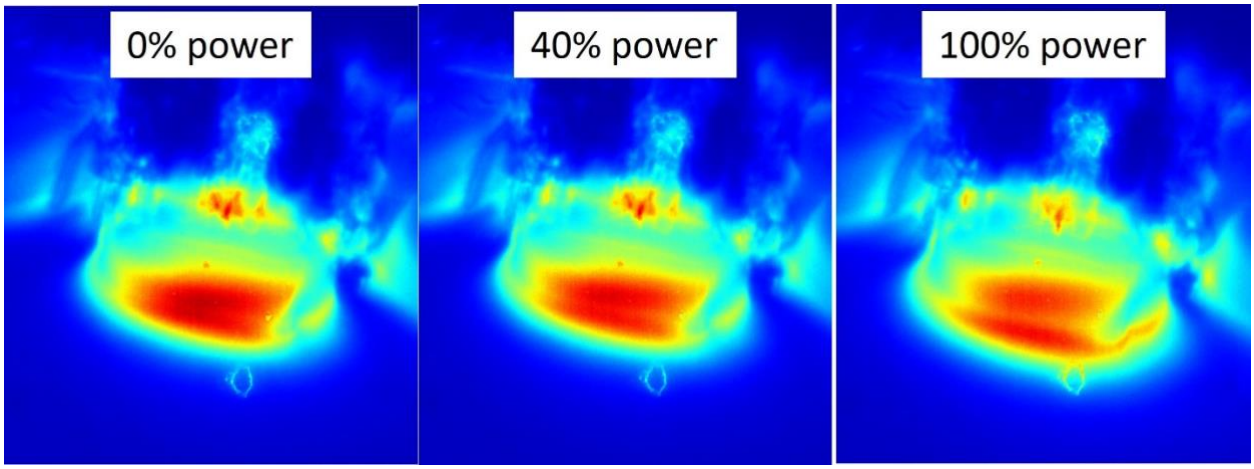

Figure 20: Evolution of the diffraction pattern for a measurement where we disabled the active cooling during the application of electrical bias on the device. The bright contrast imaged around the active region is observed to broaden with ~ 10% as the applied bias to the device is increased toward the largest values. The device facet experienced a catastrophic failure immediately after the "100% power" scan. The scale of lateral field of view is ~ 20 μm, while the vertical scale is proportionally larger with a factor of ~ 1.5 due to projection of X-rays in the scattering plane.

Near the end of our beam time, we measured reciprocal space maps of the devices near the active region and we identified one specific location in the reciprocal space that could be useful for performing future measurements (see Fig. 21). This location is next to a primary peak (we call it a "shoulder" of the primary peak) that is observed in the active region, but not in the surrounding material. We did not use this diffraction condition for systematic measurements earlier in the week, but we planned to investigate it further in follow-up visits to the lab.

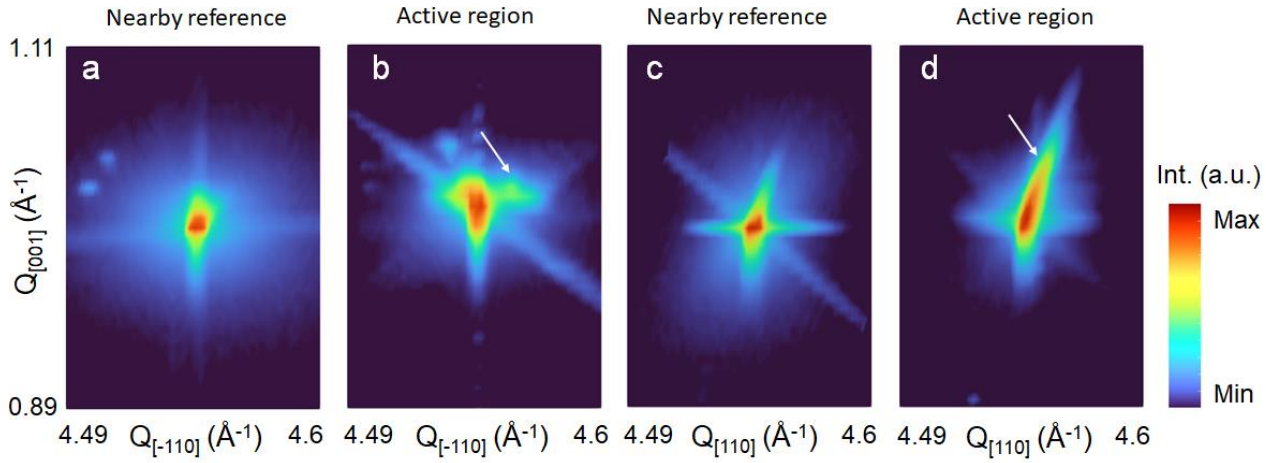

Figure 21: Reciprocal space map (RSM) images taken from the device facet, when aligned on the active region and nearby and not overlapping with the active region. The bright red peak is the 331 Bragg peak coming mostly from bulk, while additional diffuse scattering features are observed around it (relative to reference RSM's) when the X-ray beam is centered on

the active region. The white arrows indicate the position of diffuse scattering attributed to facet lattice tilts in the surface region, which are not present in the diffraction patterns of nearby references. Imaging of the lattice tilts is proposed for further investigations in future experiments. The RSM's provide diffraction patterns as a function of scattering wavevector, $Q_{[-110]}$, oriented along the surface and the long edge of the active region, and also as a function of scattering wavevector, $Q_{[110]}$, oriented perpendicular to the facet and along the perpendicular direction to the surface.

Additionally, we were able to resolve what appeared to be threading dislocations in one of our devices, Fig. 22 (left). The device material was labeled to be B200211-08-1, but we suspect that it may have been accidentally swapped with B200206-08-1. Based on prior (004) XRD measurements performed at UW Madison on the as-grown QCL wafer, we suspect that B200206-08-1 may have partially strain relaxed, which is consistent with the threading dislocations observed, Fig. 22(right).

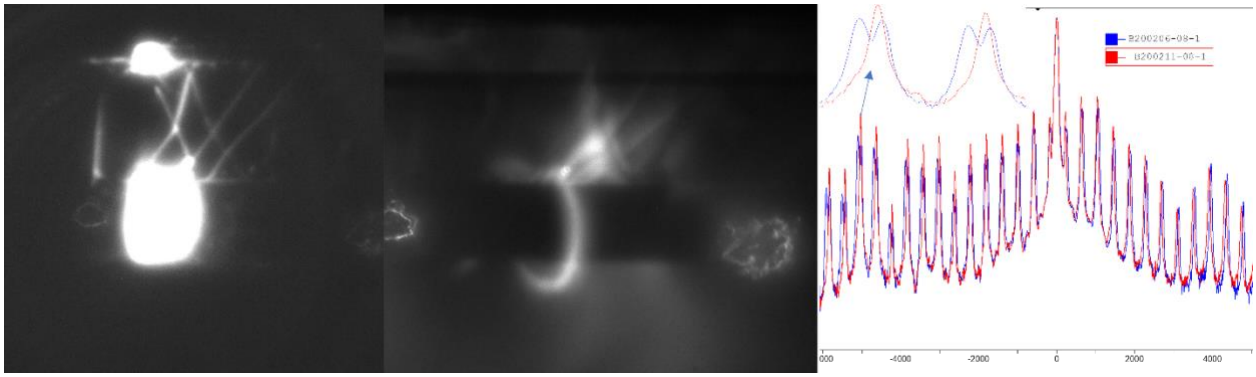

Figure 22: 220 Bragg peak XRIM images which show what appears to be a depth profile of threading dislocations. Due to the penetration depth of the incident x-rays, we are able to see features that are buried within the material, rather than relying on observations only at the surface of the material. Also shown is a 004 rocking curve that was measured at UW Madison, which shows that B200206-08-1 is expected to be relatively poor-quality material.

Other images obtained, which may be of interest for guiding future device studies, are shown in Fig 23. These images show the etch profile resulting from the formation of the buried heterostructure (Fig. 23, left) and identification of the device active region (Fig 23, right).

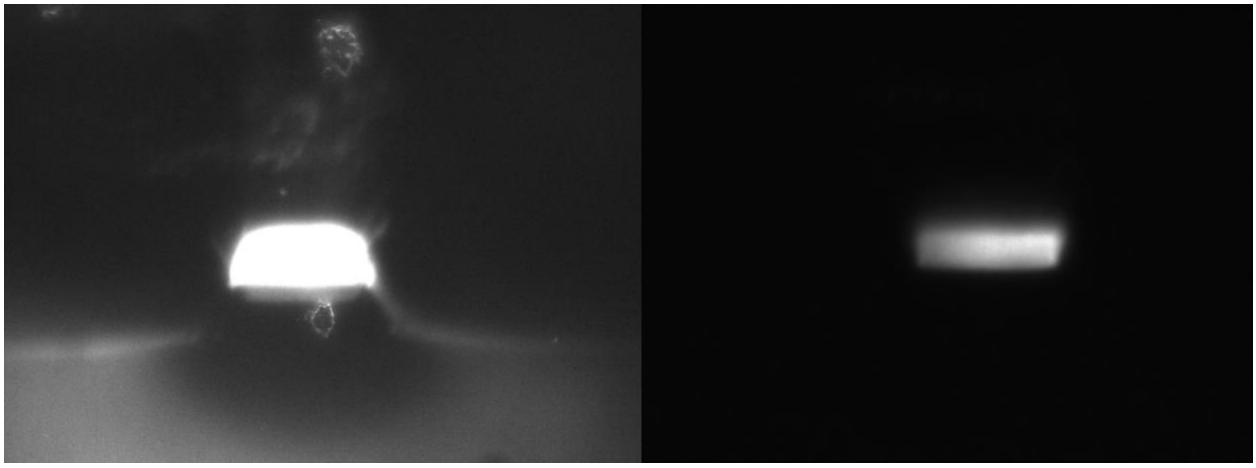

Figure 23: 33-1 Bragg peak XRIM images showing (left) the etch profile of the material and (right) the active region of the material. Keep in mind that the contrast in the images is provided by x-ray diffraction.

High resolution scanning probe microscopy of QCL devices:

Building on initial results presented in the previous section, we employed a second method imaging based of X-ray diffraction microscopy that provides a higher spatial resolution at the expense of slower measurements. For these measurements, we employed the hard X-ray nanoprobe beamline 26-ID-C from Center of Nanoscale Materials operating at the Advanced Photon Source under Argonne National Laboratory. The beamline employs a X-ray diffraction instrument operating under high vacuum for sample environment that is optimized for low -vibrations and high spatial resolution approaching 50 nm under optimized conditions. The X-ray focusing optics on the sample is a zone plate optics, focusing the X-ray beam to ~ 50 nm spot size on the sample, which is raster scanned across the surface to obtain high resolution images at specific Bragg conditions. To maximize sensitivity for imaging the active region in the surface region, we used an X-ray energy of 10.4 keV, right above the Ga absorption K-edge, which increases the absorption in the active region by a factor of 2-3 relative to smaller energies below this edge. Due to the complexity of the instrument at the beamline 26-ID-C and the restricted pace for mounting the sample, we could not apply electrical bias on the devices or perform active cooling. We therefore employed imaging of the as processed QCL structures without electrical connections. However, we explored the effect of heating the active region using a picosecond pulsed laser with energy of 1.18 eV, which is absorbing in the active region but is not absorbed in the substrate.

Before data presentation, we point out that the data analysis is complex and requires systematic reconstructions as function of small deviations from reference Bragg diffraction conditions, while are focusing here on presentation of a couple of keys preliminary experimental results. Further data analysis efforts are planned in collaboration with beamline staff, Dr. Tao Zhou and Dr. Martin Holt, and are required for a complete interpretation of the experiments.

In Fig. 24, we show the imaging results at the Bragg and near Bragg condition, which point out the origins of the imaging contrast observed in the experiments. When analyzing the tilt, y, of the diffraction peak in the vertical direction, the active region appears darker off the Bragg angle and shows successive rings at the Bragg angle. These results point the lattice bending in the facet region and imply surface swelling due to stain accumulated at the

boundary between active region and surround materials. The bright regions on the rings correspond to local variations in the scattering angle meeting the diffraction condition corresponding to a bent lattice near the surface region of the facet. Model ideas are currently being tested against the experimental data and are aimed at extracting the surface curvature as function of position across the device structure. In contrast, the lattice tilts and strains in the horizontal direction, x, are less modulated with rings present only at the prominent spatial regions where Bragg diffraction goes from bight to dark due to local bending of the lattice. These preliminary results point toward a larger lattice bending in the y direction compared to x direction.

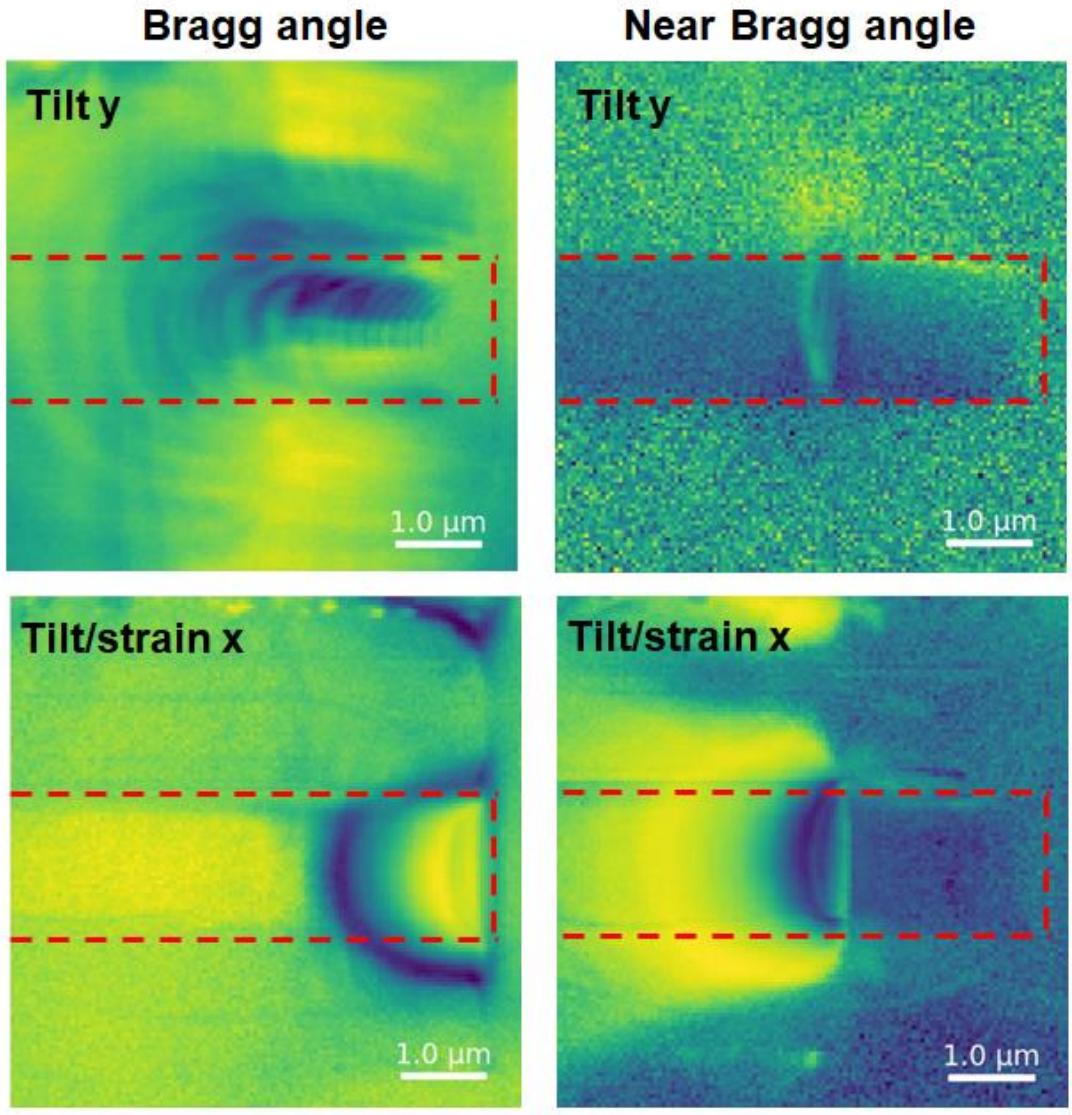

Figure 24: Hard X-ray nanoprobe imaging of QCL active region (indicated by dashed red lines) and surrounding materials for two incident angles of X-ray beam corresponding to the Bragg condition for the bulk and near it, respectively. The contrast shows spatial contrast analyzed from the peak shifts in the y (vertical) versus x (horizontal) directions. Complex imaging patterns arise to due convolution of surface and bulk scattering, including local lattice bending in the surface region.

To complement the in-operando device heating induce electrically in the previous section, we use steady state laser heating of the active region as described above, while the main result is shown in Fig. 25. By direct comparison of the tilts in the x and y directions, and strain in the x direction explored with and without laser heating, we can confirm that high resolution nanoprobe imaging also captures the enlargement of bright contrast adjoining the active region with surroundings as in XRIM probes of lattice heating. These results are attributed to changes in thermo-elastic strains and surface swelling conditions and need further analysis for confirmations.

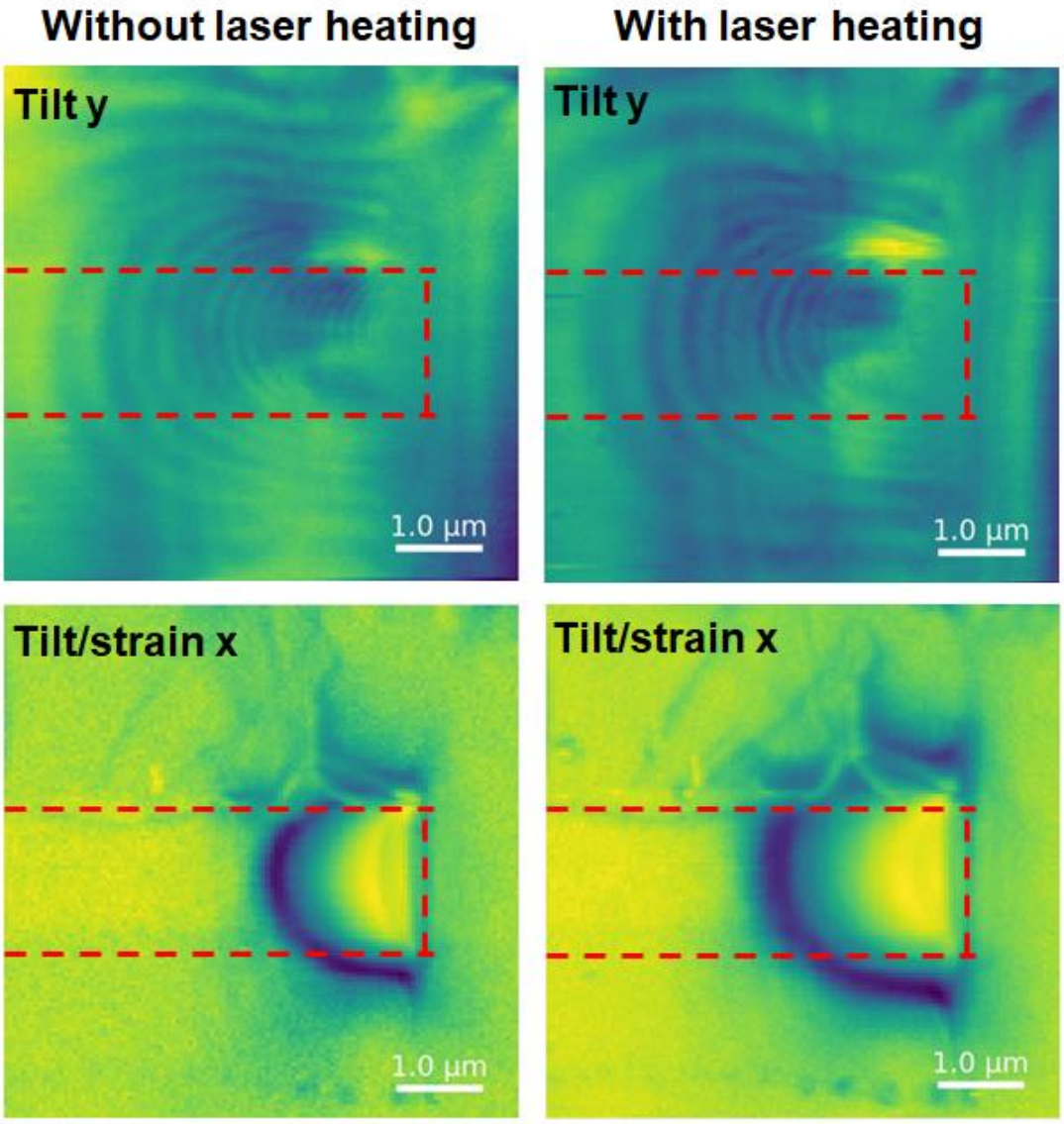

Figure 25: Hard X-ray nanoprobe imaging of QCL active region (indicated by dashed red lines) and surrounding materials for capturing the effect of an external laser heating of the active region as described in the text. The contrast shows spatial contrast analyzed from the peak shifts in the y (vertical) versus x (horizontal) directions. Complex imaging patterns arise to due convolution of surface and bulk scattering, including local lattice bending in the surface region. The extent of lattice deformations near the active region is enlarged laterally under lattice heating.

Overall, the X-ray diffraction microscopy pursued in two instrument configurations demonstrate that crucial insight can be obtained in distribution of lattice deformation in the as fabricated devices and in-situ heating and device failure observations of changes. Such results were not available previously and provide crucial insights for future optimization of QCL fabrication schemes as well as modeling of in-operando device performance.

QCL active region Microstructure Analysis:

In-plane interface roughness (IFR) values were extracted via atomic probe tomography (APT) for a few key interfaces within a quantum cascade laser (QCL) active region composed of compressively-strained InGaAs quantum wells (QWs) and AlInAs tensilely-strained barriers. The structure was grown by MOCVD at 605°C, 100 rpm, 100 torr, with a 5 second interruption time between layers. The full stage thickness measured via high-resolution x-ray diffraction (HR-XRD) is used to calibrate the reconstruction to within 5%. From the APT results, it is found that for the same compressive-strain QWs the interfaces to two barriers of different tensile-strain value (i.e., of different Al concentration) have a 50% larger RMS- roughness amplitude as the strain differential increases. To the best of our knowledge, this is the first experimental data showing that roughness parameters within a QCL active region are different for different interfaces within the same grown structure (See Table 1).

Table 1: Extracted IFR parameters and interfacial mixing width from the three interfaces of interest averaged across 3 stages. The strain is calculated at the mid-point of the change in Al concentration through the interface of interest. The column labeled Strain at the Interface is the magnitude of the strain between the compressive-strained barrier and tensile-trained well.

Interface	*Δ (nm)*	*Λ (nm)*	*Interfacial Mixing Width (nm)*	*Differential Strain Relative to InP (%)*
$In_{0.69}Ga_{0.31}As$ → $Al_{0.65}In_{0.35}As$	0.145 (±0.02)	6.61 (±0.76)	0.54 (±0.05)	2.3
$Al_{0.65}In_{0.35}As$ → $In_{0.69}Ga_{0.31}As$	0.120 (±0.01)	5.75 (±0.36)	0.61 (±0.08)	2.3
$AlAs$ → $In_{0.75}Ga_{0.25}As$	0.201 (±0.02)	7.08 (±1.06)	0.68 (±0.2)	5.1

Such IFR parameter data can be utilized in the design of QCL active regions to reduce carrier leakage and improve wallplug efficiency. Ongoing projects (Navy STTR) are using such IFR data to refine QCL active region simulation, allowing for further optimization of active region design. Characterizing the IFR parameters for all interfaces within the QCL structure will enable IFR engineering of the QCL structure for achieving further enhancements in device performance. In addition, the OMVPE growth optimization can be carried out to reduce roughness parameters for key interfaces within QCL structures.

References

[1] D.G. Cahill, W.K. Ford, K.E. Goodson, G.D. Mahan, A. Majumdar, H.J. Maris, R. Merlin, and S.R. Phillpot, J. Appl. Phys. **93**, 793 (2003).

[2] M.N. Luckyanova, J. Garg, K. Esfarjani, A. Jandl, M.T. Bulsara, A.J. Schmidt, A.J. Minnich, S. Chen, M.S. Dresselhaus, Z. Ren, E.A. Fitzgerald, and G. Chen, Science **338**, 936 (2012).

[3] M.N. Luckyanova, J. Mendoza, H. Lu, B. Song, S. Huang, J. Zhou, M. Li, Y. Dong, H. Zhou, J. Garlow, L. Wu, B.J. Kirby, A.J. Grutter, A.A. Puretzky, Y. Zhu, M.S. Dresselhaus, A. Gossard, and G. Chen, Sci. Adv. **4**, eaat9460 (2018).

[4] S.M. Lee, D.G. Cahill, and R. Venkatasubramanian, Appl. Phys. Lett. **70**, 4 (1997).

[5] T. Borca-Tasciuc, W. Liu, J. Liu, T. Zeng, D.W. Song, C.D. Moore, G. Chen, K.L. Wang, M.S. Goorsky, T. Radetic, R. Gronsky, T. Koga, and M.S. Dresselhaus, Superlattices Microstruct. **28**, 8 (2000).

[6] S.T. Huxtable, A.R. Abramson, C.-L. Tien, A. Majumdar, C. LaBounty, X. Fan, G. Zeng, J.E. Bowers, A. Shakouri, and E.T. Croke, Appl. Phys. Lett. **80**, 1737 (2002).

[7] K. Kothari, A. Malhotra, and M. Maldovan, J. Phys. Condens. Matter **31**, 345301 (2019).

[8] P. Chakraborty, I.A. Chiu, T. Ma, and Y. Wang, Nanotechnology **32**, 065401 (2021).

[9] M.V. Simkin and G.D. Mahan, Phys. Rev. Lett. **84**, 927 (2000).

[10] B.C. Daly, H.J. Maris, K. Imamura, and S. Tamura, Phys. Rev. B **66**, 024301 (2002).

[11] E.S. Landry and A.J.H. McGaughey, Phys. Rev. B **79**, 075316 (2009).

[12] K. Termentzidis, P. Chantrenne, J.-Y. Duquesne, and A. Saci, J. Phys. Condens. Matter **22**, 475001 (2010).

[13] W.S. Capinski, H.J. Maris, T. Ruf, M. Cardona, K. Ploog, and D.S. Katzer, Phys. Rev. B **59**, 8105 (1999).

[14] J. Garg and G. Chen, Phys. Rev. B **87**, 140302 (2013).

[15] J. Ravichandran, A.K. Yadav, R. Cheaito, P.B. Rossen, A. Soukiassian, S.J. Suresha, J.C. Duda, B.M. Foley, C.-H. Lee, Y. Zhu, A.W. Lichtenberger, J.E. Moore, D.A. Muller, D.G. Schlom, P.E. Hopkins, A. Majumdar, R. Ramesh, and M.A. Zurbuchen, Nat. Mater. **13**, 168 (2014).

[16] B. Saha, Y.R. Koh, J. Comparan, S. Sadasivam, J.L. Schroeder, M. Garbrecht, A. Mohammed, J. Birch, T. Fisher, A. Shakouri, and T.D. Sands, Phys. Rev. B **93**, 045311 (2016).

[17] P. Hołuj, C. Euler, B. Balke, U. Kolb, G. Fiedler, M.M. Müller, T. Jaeger, P. Kratzer, and G. Jakob, Phys. Rev. B **92**, 125436 (2015).

[18] V. Samvedi and V. Tomar, Nanotechnology **20**, 365701 (2009).

[19] M. Hu and D. Poulikakos, Nano Lett. **12**, 5487 (2012).

[20] Y. Chen, D. Li, J.R. Lukes, Z. Ni, and M. Chen, Phys. Rev. B **72**, 174302 (2005).

[21] Y. Wang, H. Huang, and X. Ruan, Phys. Rev. B **90**, 165406 (2014).

[22] L.J. Mawst and D. Botez, IEEE Photonics J. **14**, 1 (2022).

[23] A. Sood, J.A. Rowlette, C.G. Caneau, E. Bozorg-Grayeli, M. Asheghi, and K.E. Goodson, Appl. Phys. Lett. **105**, 051909 (2014).

[24] G.R. Jaffe, S. Mei, C. Boyle, J.D. Kirch, D.E. Savage, D. Botez, L.J. Mawst, I. Knezevic, M.G. Lagally, and M.A. Eriksson, ACS Appl. Mater. Interfaces **11**, 11970 (2019).

[25] S. Mei and I. Knezevic, J. Appl. Phys. **118**, 175101 (2015).

[26] B.M. Foley, H.J. Brown-Shaklee, J.C. Duda, R. Cheaito, B.J. Gibbons, D. Medlin, J.F. Ihlefeld, and P.E. Hopkins, Appl. Phys. Lett. **101**, 231908 (2012).

[27] J. Zhu, D. Tang, W. Wang, J. Liu, K.W. Holub, and R. Yang, J. Appl. Phys. **108**, 094315 (2010).

[28] J.J. Gengler, J. Hu, J.G. Jones, A.A. Voevodin, P. Steidl, and J. Vlček, Surf. Coat. Technol. **206**, 2030 (2011).
[29] H. Harikrishna, W.A. Lanford, S.W. King, and S.T. Huxtable, J. Nucl. Mater. **514**, 154 (2019).
[30] Z. Tian, A. Marconnet, and G. Chen, Appl Phys Lett 5 (2015).
[31] Z. Cheng, L. Yates, J. Shi, M.J. Tadjer, K.D. Hobart, and S. Graham, APL Mater. **7**, 031118 (2019).
[32] R.M. Costescu, M.A. Wall, and D.G. Cahill, Phys. Rev. B **67**, 054302 (2003).
[33] L.S. Larkin, M.R. Redding, N.Q. Le, and P.M. Norris, J. Heat Transf. **139**, 031301 (2017).
[34] P. Jiang, X. Qian, and R. Yang, J. Appl. Phys. **124**, 161103 (2018).
[35] A.J. Schmidt, X. Chen, and G. Chen, Rev. Sci. Instrum. **79**, 114902 (2008).
[36] D.G. Cahill, Rev. Sci. Instrum. **75**, 5119 (2004).
[37] L.N. Maurer, S. Mei, and I. Knezevic, Phys. Rev. B **94**, 045312 (2016).
[38] D. Botez, J.D. Kirch, C. Boyle, K.M. Oresick, C. Sigler, H. Kim, B.B. Knipfer, J.H. Ryu, D. Lindberg, T. Earles, L.J. Mawst, and Y.V. Flores, Opt. Mater. Express **8**, 1378 (2018).
[39] B. Knipfer, S. Xu, J.D. Kirch, D. Botez, and L.J. Mawst, J. Cryst. Growth **583**, 126531 (2022).
[40] B. Yang and G. Chen, Phys. Rev. B **67**, 195311 (2003).

Recommendations:

- Fabricate larger area Phase-Locked arrays with complete current confinement to elements: Characterization of arrays under QCW operation
- Implement 3D device modelling (in conjunction with Intraband LLC) to optimize the reverse taper geometry QCL
- Continue studies on the impact of strain on the SL thermal conductivity, higher strain investigation is needed. APT studies should be extended to encompass axial as well as lateral IFR parameter extraction.
- Extend x-ray mapping of QCL facet degradation to quantify strain fields under self-heating. This type of mapping can also be utilized to better understand the heat management in phase-locked QCL arrays.
- Continue collaboration with Irena Knezevic (UW-Madison) to develop improved models of phonon transport in QCL SLs structures, incorporating real parameters such as interfacial roughness at barrier/well interfaces.

Personnel Supported: At UW-Madison, one graduate student and one postdoc researcher were partially supported during the current reporting period.

- Shuqi Zhang, current PhD graduate student fully supported by this project
- Dr. Nikhil Pokharel, postdoc researcher (partially funded)

At Penn State University, one graduate student was supported to date by this program.

- Carlos Perez, Graduated PhD

Journal Publications:

1) Jae Ha Ryu, J. D. Kirch, B. Knipfer, Z. Lui, T. Earles, R. Marsland, A. Strömberg, G. Omanakuttan, Y.T. Sun, S. Lourdudoss, D. Botez, and L. J. Mawst, "Beam Stability of Buried-Heterostructure Quantum Cascade Lasers Employing HVPE Regrowth**",** Optics Express**,** Vol. 29, issue 2, pp. 2819-282 (2021).
2) L. J. Mawst and D. Botez, **INVITED** "High-Power Mid-Infrared (λ∼3-6 μm) Quantum Cascade Lasers," in *IEEE Photonics Journal*, vol. 14, no. 1, pp. 1-25, Feb. 2022, Art no. 1508025, doi: 10.1109/JPHOT.2021.3132261.
3) J. H. Ryu *et al*., "Reverse-Taper Mid-Infrared Quantum Cascade Lasers for Coherent Power Scaling," in *IEEE Photonics Journal*, vol. 14, no. 3, pp. 1-6, June 2022, Art no. 1522706, doi: 10.1109/JPHOT.2022.3163409.
4) C. Perez, D. Talreja, J. Kirch, S. Zhang, V. Gopalan, D. Botez, B. M. Foley, B. Ramos-Alvarado, L. J. Mawst; Time domain thermoreflectance measurements and phonon gas modeling of the thermal conductivity of silicon doped indium phosphide pertinent to quantum cascade lasers. *APL Mater* 1 April 2023; 11 (4): 041107.
5) C. Perez, L. Avazpour, M. K. Eryilmaz, T. Earles, S. Ruder, V. Gopalan, D. Botez, I. Knezevic, B. Ramos-Alvarado, B. M. Foley, and L. J. Mawst , "Incoherent-to-coherent

crossover in thermal transport through III–V alloy superlattices", Appl. Phys. Lett. 121, 232201 (2022)

6) Carlos Perez, Y. Sun, R. Lavelle, D. Botez, V. Gopalan, L. Mawst, B. M. Foley, "Thermal Conductivity of Fe-doped InP Grown Via Halide Vapor Phase Epitaxy", *In Preparation*
7) B. Knipfer, S. Xu, J.D. Kirch, D. Botez, L.J. Mawst, Analysis of interface roughness in strained InGaAs/AlInAs quantum cascade laser structures (λ ∼ 4.6 μm) by atom probe tomography, Journal of Crystal Growth, Volume 583, 126531, 2022.

Conference Presentations:

Invited

1. **Luke J. Mawst**, Jae Ha Ryu, Jeremy D. Kirch, Shining Xu, Morgan Turville-Heitz, Shuqi Zhang, Suraj Suri, Dan Botez, Benjamin Knipfer, Robert A. Marsland, Steve Jacobs, Axel Strömberg,Yan-Ting Sun, Sebastian Lourdudoss, Tom Earles, Steven Ruder, Kevin Oresick, Chris Galstad, Michael Klaus, "High-Power Mid-IR Quantum Cascade Lasers grown by MOCVD", Australian Institute of Physics Congress; COMMAD 2022, Adelaide, Australia, Dec. 2022.
2. **Luke J. Mawst**, Jae Ha Ryu, Jeremy D. Kirch, Shining Xu, Morgan Turville-Heitz, Shuqi Zhang, Suraj Suri, Dan Botez, Benjamin Knipfer, Robert A. Marsland, Steve Jacobs, Axel Strömberg,Yan-Ting Sun, Sebastian Lourdudoss, Tom Earles, Steven Ruder, Kevin Oresick, Chris Galstad, Michael Klaus, "Monolithic Coherent Power Scaling of Mid-IR Quantum Cascade Lasers", SPIE Photonics West, San Francisco, CA, Jan. 2023

Contributed

1. B. Knipfer, S. Xu, J.D. Kirch, D. Botez, and L.J. Mawst, "Analysis of Interfacial Roughness of Strained InGaAs/AlInAs QCLs (λ~4.6um) by Atom Probe Tomography" AACG-22/OMVPE-20, August 2021, virtual conference.

2. Jae Ha Ryu, Jeremy D. Kirch, Benjamin Knipfer, Zerui Liu, Morgan TurvilleHeitz, Tom Earles, Robert A. Marsland, Axel Strömberg, Giriprasanth Omanakuttan, Yan-Ting Sun, Sebastian Lourdudoss, Dan Botez, Luke J. Mawst, "Beam stability of buried-heterostructure quantum cascade lasers formed by ICP-etching and HVPE regrowth," SPIE-Photonics West, Novel In-Plane Semiconductor Lasers XX, March 2021, virtual conference.

3. Jae Ha Ryu, Benjamin Knipfer, Jeremy D. Kirch, Robert A. Marsland, Steve Jacobs, Dan Botez, Tom Earles, Morgan Turville-Heitz, Chris Sigler, Axel Strömberg,Yan-Ting Sun, Sebastian Lourdudoss, and Luke J. Mawst, "Reverse-Taper Mid-IR Quantum Cascade Lasers for Coherent Power Scaling", IEEE ISLC, virtual conference, Oct. 2021

4. Shuqi Zhang, Jae Ha Ryu, Jeremy D. Kirch, Dan Botez, Luke J. Mawst, Tom Earles, Steven Ruder, Improved Current Injection for Resonant Leaky-Wave Coupled Arrays of Mid-Infrared Quantum Cascade Lasers, IEEE Photonics Conference, Nov. 2023.

Honors/Awards during project:

For L. J. Mawst

- IEEE Photonics Society Aron Kressel Award, 2019
- UW-Madison Grainger Professorship (2022)